Spring 1-1-2013

Negating the Yearly Eccentricity Magnitude Variation of Super-synchronous Disposal Orbits due to Solar Radiation Pressure

Stephanie Leigh Jones
University of Colorado at Boulder, sljase@gmail.com

Negating the Yearly Eccentricity Magnitude Variation of Super-synchronous Disposal Orbits due to Solar Radiation Pressure

by

S. L. Jones

B.S., The University of Texas at Austin, 2011

A thesis submitted to the

Faculty of the Graduate School of the

University of Colorado in partial fulfillment

of the requirements for the degree of

Master of Science

Department of Aerospace Engineering Sciences

2013

This thesis entitled:
Negating the Yearly Eccentricity Magnitude Variation of Super-synchronous Disposal Orbits due to Solar Radiation Pressure
written by S. L. Jones
has been approved for the Department of Aerospace Engineering Sciences

_____
Hanspeter Schaub

_____
Dr. Penina Axelrad

_____
Dr. Jeffrey Parker

Date _____

The final copy of this thesis has been examined by the signatories, and we find that both the content and the form meet acceptable presentation standards of scholarly work in the above mentioned discipline.

Jones, S. L. (M.S., Aerospace Engineering Sciences)

Negating the Yearly Eccentricity Magnitude Variation of Super-synchronous Disposal Orbits due to Solar Radiation Pressure

Thesis directed by Dr. Hanspeter Schaub

As a satellite orbits the Earth, solar radiation pressure slowly warps its orbit by accelerating the satellite on one side of the orbit and decelerating it on the other. Since the Earth is rotating around the Sun, this perturbation cancels after one year for geostationary satellites. However, during the year the eccentricity, and therefore the radius of periapsis, changes. Since disposed geostationary satellites are not controlled, traditionally they must be reorbited higher than otherwise to compensate for this change, using more fuel. This issue has increased interest in specialized orbits that naturally negate this eccentricity perturbation. The disposal orbit examined in this thesis points its perigee toward the Sun and has a natural eccentricity based on the satellite's parameters. This converts the eccentricity vector derivative due to solar radiation pressure into a directional change only, keeping the eccentricity magnitude, and the radius of periapsis, constant. A constant radius of periapsis reduces the necessary semi-major axis for the disposal orbit, and therefore the fuel needed to reorbit the satellite.

This thesis examines this disposal orbit and the solar radiation perturbation over a single year. First, the solar radiation pressure yearly perturbation is derived from Gaussian variational equations. This process validates the eccentricity vector behavior and gives useful insights into its cause. After the derivation, the perturbation behavior is modeled in MATLAB for the proposed disposal orbit. The traditional and proposed disposal orbits are also modeled used NASA's General Mission Analysis Tool to show the modified orbit behavior in a more realistic setting.

After the proposed disposal orbit's radius of periapsis behavior is verified, its sensitivity to various satellite parameters is analyzed. Solar radiation pressure, reflectivity, area, mass, initialization, and perigee offset errors are examined. Analytical relationships are developed for these

sensitivities to show their effects on the minimum radius of the periapsis over one year. This thesis shows that while this orbit modification can be used to modify orbits in the short term, margins should be included depending on uncertainties in the satellite parameter knowledge to guarantee minimum altitude above the geostationary belt.

Dedication

I would like to dedicate this thesis to all my friends and family, who have been so supportive of me throughout this incredible process.

Acknowledgements

First and foremost, I want to acknowledge my advisor. Dr. Hanspeter Schaub has been extremely supportive of my education and research at The University of Colorado. Without his help and advice this thesis will not be possible. I also want to thank both Dr. Penina Axelrad and Dr. Jeffrey Parker for their time and insights as committee members. In addition, I want to acknowledge the engineers and scientists who have contributed to the awareness and prevention of space debris. Their research is not only the basis for this thesis, but fundamental for future space operations. Last but not least, I want to thank my friends and family for their endless encouragement. I especially wish to thank my parents, who have always been there for me. There are not enough words to express my gratitude to you both.

Contents

Chapter

Tables

Table

Figures

Figure

Chapter 1

Introduction

1.1 Space Debris Situation

According to the Inter-Agency Space Debris Coordination Committee (IADC), space debris is defined as "all man made objects including fragments and elements thereof, in Earth orbit or re-entering the atmosphere, that are non functional" [8]. As more and more satellites are launched into space, the risk of debris from collisions grows [17]. The first observed collision was in 1996, where a piece from an Ariane upper stage damaged Cerise, a French-owned minisatellite [8, 18, 19]. Evidence of the true seriousness of this problem can be seen in the February 11, 2009, collision between an Iridium satellite and an inactive Russian Cosmos 2251 spacecraft [10, 17]. This collision was not predicted and created two large groups of space debris [17]. Some scientists believe in Donald Kessler's theory of "collisional cascading", or "Kessler Syndrome", which suggests that at a certain point a collision will trigger further collisions until the Earth is surrounded by debris and space is no longer accessible for operations [8, 17, 19]. Although so far the only collisions have been in low-Earth orbit (LEO), the danger exists for all satellites. Even small debris can damage satellites, which can lead to their early demise or reduced satellite control [8, 19].

Even though satellites are assigned positions in space, the risk continues to rise, especially in regions with more satellites [10, 17, 19]. In addition, there is not enough equipment and manpower available to track all of the debris [17]. Current instrumentation can only regularly track objects greater the ten centimeters in LEO and one meter in geostationary orbit (GEO) [5, 8, 10, 17]. As technology improves, it is expected that the perceived scope of the space debris problem will

increase [6, 7]. Assess to data is also an issue since some satellites are classified [17].

As this problem becomes more recognized, focus has shifted to accurate prediction of collision risk, minimization of new debris, and management of existing debris [4, 8, 17, 18]. Satellites in LEO are deorbited (either manually or due to atmospheric drag) [7, 17]. However, satellites in GEO are too far above the Earth to be deorbited. Instead, these satellites are sent into "graveyard orbits" above the GEO belt to avoid active GEO satellites [17].

1.2 Geostationary Satellite Background

Geostationary satellites stay directly above the same point on the Earth, which means they are in circular orbits above the equator with a period of one sidereal day [10, 12, 17, 21]. Since these satellites are stationary with respect to the Earth, they are ideally suited for such tasks as communication and weather-observation [8, 10]. The first GEO satellite was launched in 1964, and the first explosion in GEO occurred in 1978 [8]. Even though no collisions have occurred to date in GEO, the battery casing of an Ekran satellite was observed breaking apart into pieces of debris [10].

As seen in Fig. 1.1 (courtesy of NASA's Orbital Debris Program Office [15]), there are a number of objects in and around the GEO belt. Note the GEO ring is visible in the figure. While these satellites are generally designed to last a long time (an average of fifteen years), they do eventually die [10]. As of January 2005, DISCOS (an European Space Agency database) listed 1124 objects in the geostationary region, but only 346 of these were actively controlled satellites. Inactive satellites numbered 549, either within or passing through the GEO belt. The remainder had too little information to be tracked properly. [7].

The practice of using a disposal orbit has existed since 1977, when Perek proposed the idea and INTELSAT sent the first satellite to one. Numerous standards have been formed by different agencies [7]. In the United States, the Federal Communications Commission will not license a satellite without an approved plan for its end-of-life, but it does not assign a minimum disposal altitude for geostationary satellites [10]. The most widely acknowledged standard today

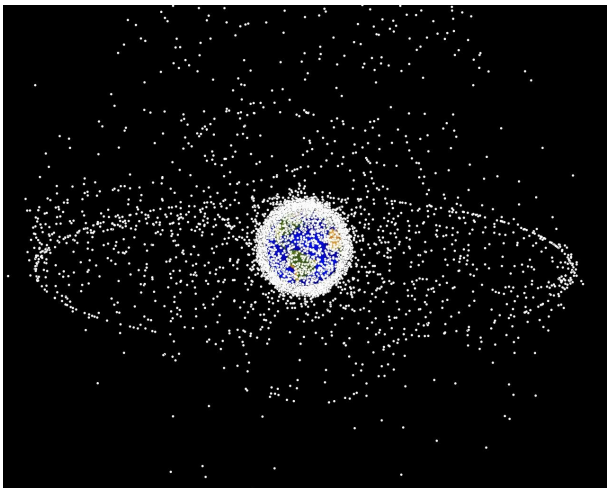

Figure 1.1: GEO Image of Space Objects [15]

was developed in 1997 by the IADC [6, 7]. It accounts for the fact that at GEO, the main perturbing effects on a satellite's orbit are solar radiation pressure and third body gravitational attractions from the Sun and Moon [21]. It also acknowledges that cross-sectional area is more of a factor at GEO because geostationary satellites comprise the largest portion of current orbiting area due to their large appendages [8]. The total increase in altitude (ΔH) is shown in Eq. (1.1), where ρ is the reflectivity (a.k.a. the solar radiation pressure coefficient), A is the average cross-sectional area of the satellite visible by the Sun in m^2, and m is the mass of the satellite in kg. [4, 6, 7, 8, 13]. The minimum reorbit altitude above GEO is set at 235 km plus an additional solar pressure term [6, 7]. The 235 km includes a 200 km minimum above the GEO belt for active satellite operations and maneuvers and 35 km for Earth and third body gravitational perturbations [4, 6, 7, 8, 13]. The protected 200 km zone also covers inclinations from $-15°$ to $15°$ [4, 13].

$$\Delta H = 200 \text{ km } + 35 \text{ km } + 1000\frac{\rho A}{m} \text{ km} \tag{1.1}$$

However, only about a third of the satellites in GEO have followed this recommended reorbit plan. From 1997 to 2004, 117 spacecraft became inactive, but only 39 were reorbited properly. Another 41 were reorbited below the minimum requirements, and 37 were left in the GEO belt [7]. This is partly because even though the IADC standard is internationally agreed upon there is no

enforcement, especially since more and more satellites are owned by private companies (although some reorbit to protect their active satellites and prevent economic loss) [10, 18]. In addition, many of the satellites launched before 1990 were not reorbited [7]. Another contributing factor is that some satellite operators only budget the absolute minimum fuel (or less) for reorbiting [6]. The cheapest way (fuel-wise) to reorbit under the IADC recommendation is to target a circular orbit of this radius. However, this must include extra height to compensate for the solar radiation perturbation, which can be as large as 50 kilometers [4].

1.3 Solar Radiation Pressure Yearly Eccentric Perturbation

As shown in Eq. (1.1), solar radiation pressure must be considered when defining a disposal orbit. All satellites in orbit around the Earth are exposed to sunlight. Photons from the Sun have linear momentum that is transferred to the satellite upon contact [23]. This creates a nonconservative force, described in Eq. (1.2), that acts on the satellite system [21]. The force of solar radiation on the spacecraft is equal to the product of the solar pressure at Earth's distance from the Sun ($p_\odot$), the reflectivity of the satellite's surface (ρ), the area of the satellite perpendicular to the radiation of the Sun (A), and a scaling factor of the distances of the Earth and satellite to the Sun ($r_\oplus/r$) [1, 23].

$$F_\odot = p_\odot \rho A \left(\frac{r_\oplus}{r}\right)^2 = m a_\odot \tag{1.2}$$

Due to the scope of this thesis, the area is taken to be the average area incident to the Sun. In reality, it changes because the attitude is not controlled, causing solar radiation to produce a changing force as well as a torque on the satellite. The assumption that the area is averaged also allows the assumption that the incidence angle is 0°, so its effect can be ignored in this analysis [21]. Note that for Earth GEO orbits, the scale factor is assumed to be one since the distance from the satellite to the Earth is much less than the distance form the Earth to the Sun. Equation (1.2) leads to the ballistic radiation coefficient (BC), shown in Eq. (1.3), which is formed from the satellite

parameters of the solar pressure acceleration [23].

$$BC = \frac{\rho A}{m} \tag{1.3}$$

The main perturbation that results from solar radiation pressure is a yearly variation in the eccentricity vector [4, 11, 12, 23]. The solar radiation pressure slightly accelerates the satellite as it travels away from the Sun and slightly decelerates it as it travels toward the Sun [12, 23]. This slowly changes the eccentricity vector [12]. If one starts with a circular orbit, it will become eccentric as shown (not to scale) in Fig. 1.2 [12, 23]. However, as the Earth rotates about the Sun, the acceleration vector from the Sun rotates about the Earth, changing the direction of the solar radiation force relative to the orbit. The result is that the eccentricity vector returns to its initial state after one orbit of the Earth around the Sun [12, 21]. This is because satellites in GEO are almost continuously exposed to sunlight since they are so far out from the Earth [11].

This can be difficult to picture intuitively. Another way of looking at this perturbation is in the eccentricity plane, shown in Fig. 1.3. The axes of this plane are formed from the modified eccentricity values $e_x = e\cos(\Omega + \omega)$ and $e_y = e\sin(\Omega + \omega)$. The traditional orbital elements used to create these are eccentricity (e), right ascension of the ascending node (Ω), and argument of periapsis (ω). In this plane, the eccentricity vector traces a circle over one year [4, 13]. As seen in Fig. 1.3, the location of the eccentricity vector on this circle is determined by α, which is the right

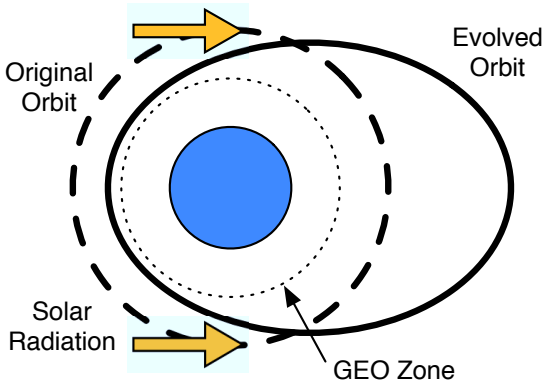

Figure 1.2: Evolution of Traditional Disposal Orbit

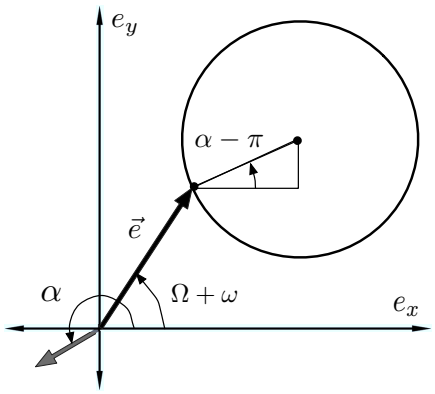

Figure 1.3: Eccentricity Vector in Eccentricity Plane

ascension of the Sun. As discussed later in this thesis, the radius of this eccentricity circle is the natural eccentricity. [12]

Note from Fig. 1.3 that for the traditional disposal orbit, starting at a null initial eccentricity leads to a maximum eccentricity that is twice the natural eccentricity. This increase in eccentricity decreases the radius of periapsis, which is why the third term of the IADC recommendation exists. (This behavior always exists in the GEO belt, but orbit maintenance for active GEO operations often overshadows it [23].) This perturbation has been used occasionally for tasks such as station-keeping, but recently it has been the focus of a new GEO disposal orbit proposed by operators of an EADS Astrium Eurostar 2000 satellite [4, 12, 13].

1.4 Thesis Focus

1.4.1 Initial Solar Radiation Pressure Perturbation Examination

This solar radiation pressure effect is widely reported among astronautical texts, but in a brief, qualitative manner. The first objective of this thesis is to rigorously examine this perturbation analytically and numerically. To this end, a full mathematical derivation from Gaussian variational equations is presented, as well as MATLAB and NASA's General Mission Analysis Tool (GMAT) simulations. The second objective of this thesis is to verify the proposed GEO disposal orbit, so

particular attention is paid to the contrast between the traditional disposal orbit dictated by the IADC and the proposed disposal orbit.

In the proposed orbit analyzed in this study, the natural eccentricity is targeted as the eccentricity magnitude, while the eccentricity vector is pointed toward the Sun. Over the year, the eccentricity vector will trace a circle centered on the eccentricity plane's origin. This means the eccentricity magnitude, and therefore the radius of periapsis, will stay constant. This is shown (not to scale) in Fig. 1.4(a). In other words, the orbit maintains the same ellipse, but rotates so that it remains pointing toward the Sun, as shown (not to scale) in Fig. 1.4(b) [4, 13].

1.4.2 Sensitivity Analysis

Once the solar radiation pressure perturbation has been rigorously analyzed and the proposed orbit has been verified, attention is turned to the sensitivity of this orbit to various parameters. The third objective of this thesis is to analyze the proposed orbit's sensitivity to solar radiation pressure, reflectivity, cross-sectional area, mass, initialization errors, and perigee-pointing offsets. These parameters are difficult to know and control accurately for satellites in orbit. These sensitivities

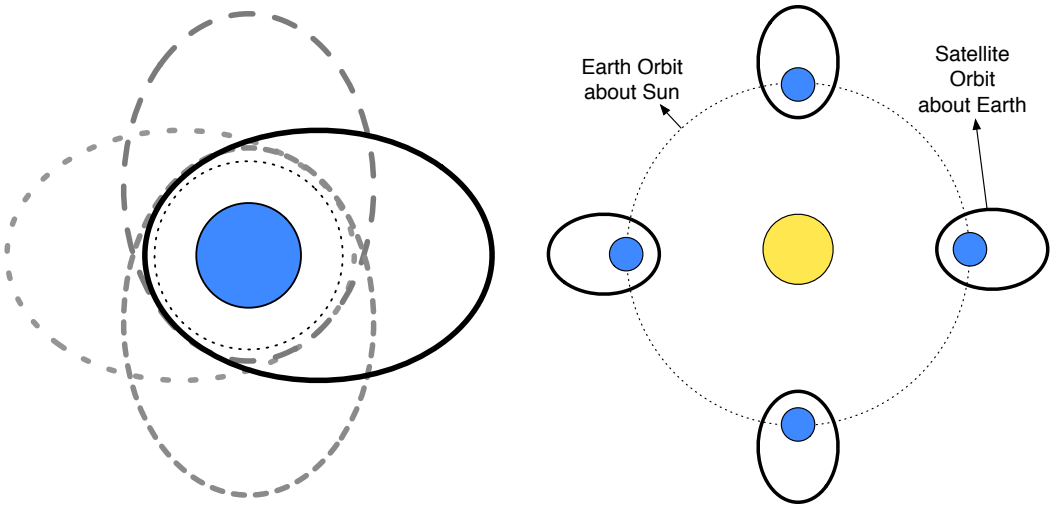

(a) Earth View (b) Sun View

Figure 1.4: Evolution of the Proposed Disposal Orbit

are analyzed with respect to the minimum radius of periapsis in both qualitative and quantitative form. To the author's knowledge, this has not been rigorously examined before for the proposed orbit. Numerous insights into the origins of solar radiation pressure's effect on orbit evolution and applicability of the proposed orbit are found in the process of this analysis.

1.4.3 Overall Context of Analysis

The research in this thesis grants insight into disposal orbit behavior and a new potential solution. However, one thesis cannot hope to complete a task such as redesigning a disposal orbit by itself. This section addresses factors outside the scope of this thesis to put it in the context of overall orbit stability.

1.4.3.1 Assumptions

There are a number of assumptions used in this analysis. While GMAT simulations show these to be small deviations, they still must be noted. The Sun is treated as moving on the equatorial plane, when in fact its average motion is on the ecliptic plane [21, 23]. The ecliptic plane is inclined 23.44° from the equatorial plane [12], so there is a slight out-of-plane acceleration from solar radiation pressure [23]. The cosine of this angle is 0.9175, so this assumption is acceptable for the in-plane behavior. GMAT simulations show the out-of-plane effect, along with other perturbations, to be smaller than the analyzed behavior. The Earth's orbit about the Sun is also assumed circular, which is a common assumption since the Earth's orbit actually has an eccentricity of 0.0167 [12, 21].

1.4.3.2 Longer-Term Evolution

The proposed orbit has not yet been addressed specifically for long-term evolution. However, general studies on long-term stability of super-synchronous orbits (SSO) have found some generic results. For IADC disposal orbits, the eccentricity magnitude needs to be smaller than 0.005 for long-term evolution (natural eccentricities are generally less than this) [3, 8, 9, 23]. Interestingly, some studies have shown that pointing the disposal orbit's perigee toward the Sun is also good

for long-term evolution [3]. On the other hand, some studies have shown that perigees close to the GEO protected zone are more likely to enter it in the future, but no data was given for which eccentricity vectors these violators had [9].

Periodic variations in eccentricity have also been observed for longer periods due to a variety of sources such as third body gravitational attractions, but no secular perturbations occur [2, 3]. GEO satellites also have a long-term perturbation of 53 years that shifts their inclinations between $-15°$ and $15°$. This is due to gravitational perturbations from the Earth, the Sun, and the Moon [8]. This indirectly affects the solar radiation pressure perturbation by changing how much of the solar radiation force acts in the orbit plane.

Chapter 2

Proposed Orbit Yearly Evolution Derived from Gaussian Variational Equations

To examine the proposed orbit's effect on the solar radiation pressure eccentricity perturbation in a more rigorous manner, first analyze the proposed orbit mathematically. To do so, a new set of coordinates must be assigned to properly address the highly-circular nature of GEO disposal orbits. Since the main focus of this study is the eccentricity vector, this analysis will focus on these elements. The traditional orbital elements are the semi-major axis (a), eccentricity (e), inclination (i), right ascension of the ascending node (Ω), argument of periapsis (ω), and true anomaly (θ) [21]. The first and last of these are kept, but the middle four are combined into the new orbital elements shown in Eq. (2.1) [4, 12].

$$\begin{aligned} e_x &= e\cos(\Omega+\omega) \\ e_y &= e\sin(\Omega+\omega) \\ i_x &= i\cos(\Omega+\omega) \\ i_y &= i\sin(\Omega+\omega) \end{aligned} \tag{2.1}$$

This traces a full circle for $\alpha = \Omega + \omega = 0$ to 2π radians, which is equivalent to one year. To mathematically analyze this case, Gaussian variational equations are used to more intuitively examine this behavior since the force is nonconservative. Note that while there are numerical integration issues for some Gaussian variational equations with circular orbits [21], general eccentricity behavior is analytically examined here without numerical integration.

The relevant Gaussian variational equations that calculate the orbital element derivatives

with respect to time due to a perturbing acceleration are shown in Eq. (2.2), where h is the angular momentum of the satellite, μ is the gravitational parameter of the Earth, a_r is the radial solar pressure acceleration, a_θ is the cross-radial solar pressure acceleration, a_h is the solar pressure acceleration perpendicular to the orbit plane, and r is the distance of the satellite from the satellite to the center of the Earth [23].

$$\begin{aligned}
\dot{e} &= \frac{h}{\mu}\left(\sin\theta a_r + \left(\frac{e+\cos\theta}{1+e\cos\theta}+\cos\theta\right)a_\theta\right) \\
\dot{\omega} &= \frac{h}{e\mu}\left(-\cos\theta a_r + \left(\frac{2+e\cos\theta}{1+e\cos\theta}\right)\sin\theta a_\theta\right) - \frac{r\sin(\theta+\omega)\cos i a_h}{h\sin i} \\
\dot{\Omega} &= \frac{r\sin(\theta+\omega)a_h}{h\sin i}
\end{aligned} \tag{2.2}$$

2.1 Perigee aligned with Sun Setup

When the orbit's perigee is aligned with the Sun as seen in Fig. 2.1, $a_r = a_\odot(-\cos\theta)$, $a_\theta = a_\odot(\sin\theta)$, and $a_h = 0$ (where $a_\odot$ is the magnitude of the solar pressure acceleration). Using these acceleration terms, Eq. (2.2) is simplified to Eq. (2.3).

$$\begin{aligned}
\dot{e} &= \frac{ha_\odot}{\mu}\left(\frac{e+\cos\theta}{1+e\cos\theta}\right)\sin\theta \\
\dot{\omega} &= \frac{ha_\odot}{e\mu}\left(1+\left(\frac{\sin^2\theta}{1+e\cos\theta}\right)\right) \\
\dot{\Omega} &= 0
\end{aligned} \tag{2.3}$$

Also note that $\alpha = \Omega + \omega$ when the satellite orbit's perigee is aligned with the Sun.

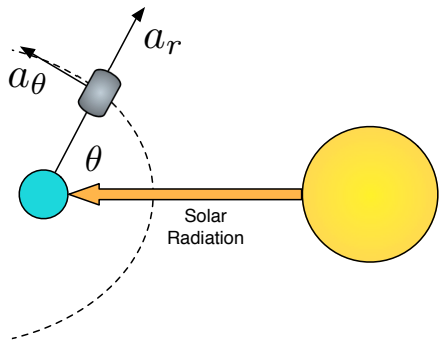

Figure 2.1: Perigee-Aligned Solar Pressure Force

2.2 Derivation of Ideal $\dot{e}_x$

The period of the examined eccentricity perturbation is one year. To approximate the derivative for this, evaluate the change in these parameters over one orbit around the Earth of time length T (one sidereal day for GEO). Start with Eq. (2.4) [12].

$$\delta e_x = \int_0^T \left(\dot{e} \cos(\Omega + \omega) - e \left(\dot{\Omega} + \dot{\omega} \right) \sin(\Omega + \omega) \right) \mathrm{d}t \tag{2.4}$$

Substituting Eq. (2.3) into Eq. (2.4) gives Eq. (2.5).

$$\begin{aligned} \delta e_x &= \frac{h \cos(\Omega + \omega) a_\odot}{\mu} \int_0^T \left(\frac{e + \cos\theta}{1 + e\cos\theta} \right) \sin\theta \mathrm{d}t \\ &\quad - \frac{h \sin(\Omega + \omega) a_\odot}{\mu} \int_0^T \left(1 + \frac{\sin^2\theta}{1 + e\cos\theta} \right) \mathrm{d}t \end{aligned} \tag{2.5}$$

Since the eccentricity is so small, it is only taken to the first order. This type of approximation is common in general perturbation analysis. While it does introduce a slight error, it allows easier observance of the dominating behavior [21]. Therefore Eq. (2.5) is expanded into Eq. (2.6), which is simplified into Eq. (2.7).

$$\begin{aligned} \delta e_x &= \frac{h \cos(\Omega + \omega) a_\odot}{\mu} \int_0^T (e + \cos\theta)(1 - e\cos\theta) \sin\theta \mathrm{d}t \\ &\quad - \frac{h \sin(\Omega + \omega) a_\odot}{\mu} \int_0^T \left(1 + \frac{\sin^2\theta}{1 + e\cos\theta} \right) \mathrm{d}t \end{aligned} \tag{2.6}$$

$$\begin{aligned} \delta e_x &= \frac{h \cos(\Omega + \omega) a_\odot}{\mu} \int_0^T \left(e + \cos\theta - e\cos^2\theta \right) \sin\theta \mathrm{d}t \\ &\quad - \frac{h \sin(\Omega + \omega) a_\odot}{\mu} \int_0^T \left(1 + \frac{\sin^2\theta}{1 + e\cos\theta} \right) \mathrm{d}t \end{aligned} \tag{2.7}$$

Next, the integral is switched from being taken over time to being taken over the true anomaly. To do this, a relationship between $\mathrm{d}t$ and $\mathrm{d}\theta$ is developed. Note that $h = r^2\dot{\theta}$ is combined with $r = \frac{h^2}{\mu(1+e\cos\theta)}$ to form Eq. (2.8) [21, 23].

$$\dot{\theta} = \frac{h}{r^2} = \frac{\mu^2 (1 + e\cos\theta)^2}{h^3} \tag{2.8}$$

Equation (2.9) is developed by using the geometric series with d taken to the first order [20].

$$\frac{1}{(1-d)^2} = \sum_{k=1}^{\infty} k d^{k-1} \sum_{k=1}^{\infty} k d^{k-1} = (1 + d + \cdots)(1 + d + \cdots) = 1 + 2d + \cdots \tag{2.9}$$

Equation (2.8) is simplified using Eq. (2.9) to get Eq. (2.10).

$$\mathrm{d}t = \frac{h^3}{\mu^2}\frac{d\theta}{(1+e\cos\theta)^2} = \frac{h^3}{\mu^2}(1-2e\cos\theta)\mathrm{d}\theta \tag{2.10}$$

Plug Eq. (2.10) into Eq. (2.7), to get Eq. (2.11), which is simplified to Eq. (2.12).

$$\begin{aligned}\delta e_x &= \frac{h^4\cos(\Omega+\omega)a_\odot}{\mu^3}\int_0^{2\pi}\left(e\sin\theta+\sin\theta\cos\theta-e\cos^2\theta\sin\theta\right)(1-2e\cos\theta)\mathrm{d}\theta \\ &\quad -\frac{h^4\sin(\Omega+\omega)a_\odot}{\mu^3}\int_0^{2\pi}\left(1+\frac{\sin^2\theta}{1+e\cos\theta}\right)(1-2e\cos\theta)\mathrm{d}\theta\end{aligned} \tag{2.11}$$

$$\begin{aligned}\delta e_x &= \frac{h^4\cos(\Omega+\omega)a_\odot}{\mu^3}\int_0^{2\pi}\left(e\sin\theta+\sin\theta\cos\theta-3e\cos^2\theta\sin\theta\right)\mathrm{d}\theta \\ &\quad -\frac{h^4\sin(\Omega+\omega)a_\odot}{\mu^3}\int_0^{2\pi}\left(1+\frac{\sin^2\theta-2e\sin^2\theta\cos\theta}{1+e\cos\theta}-2e\cos\theta\right)\mathrm{d}\theta\end{aligned} \tag{2.12}$$

This is solved as Eq. (2.13), which is evaluated as Eq. (2.14) [20].

$$\begin{aligned}\delta e_x &= \frac{h^4\cos(\Omega+\omega)a_\odot}{\mu^3}\left(-e\cos\theta|_0^{2\pi}+0.5\int_0^{2\pi}\sin 2\theta\mathrm{d}\theta-3e\int_0^{2\pi}(\sin\theta-\sin^3\theta)\mathrm{d}\theta\right) \\ &\quad -\frac{h^4\sin(\Omega+\omega)a_\odot}{\mu^3}\int_0^{2\pi}\left(1+\sin^2\theta(1-2e\cos\theta)(1-e\cos\theta)-2e\cos\theta\right)\mathrm{d}\theta\end{aligned} \tag{2.13}$$

$$\begin{aligned}\delta e_x &= \frac{h^4\cos(\Omega+\omega)a_\odot}{\mu^3}\left(-0.25\cos\theta+3e\cos\theta-e\cos\theta(\sin^2\theta+2)\right)|_0^{2\pi} \\ &\quad -\frac{h^4\sin(\Omega+\omega)a_\odot}{\mu^3}\int_0^{2\pi}\left(1-2e\cos\theta+\sin^2\theta-3e\cos\theta\sin^2\theta\right)\mathrm{d}\theta\end{aligned} \tag{2.14}$$

Note that since the first term in Eq. (2.14) is evaluated to be zero, Eq. (2.15) is true for the perigee-aligned case.

$$\int_0^T \dot{e}\mathrm{d}t = 0 \tag{2.15}$$

To continue with the derivation, solve for the integrals in Eq. (2.14) to get Eq. (2.16) [20].

$$\begin{aligned}\delta e_x &= -\frac{h^4\sin(\Omega+\omega)a_\odot}{\mu^3}\left(\theta-2e\sin\theta+0.5\theta-0.25\sin 2\theta-e\sin^3\theta\right)|_0^{2\pi} \\ &= -\frac{3\pi h^4\sin(\Omega+\omega)a_\odot}{\mu^3}\end{aligned} \tag{2.16}$$

The e_x derivative is approximated using this result for one satellite orbit in Eq. (2.17). This is possible because one day (the satellite's orbit about the Earth) is sufficiently smaller than one year

(the Earth's orbit around the Sun).

$$\frac{\mathrm{d}e_x}{\mathrm{d}\theta} = \frac{\delta e_x}{2\pi} = -\frac{3h^4 \sin(\Omega+\omega) a_\odot}{2\mu^3} \tag{2.17}$$

Substituting Eq. (1.2) into Eq. (2.17) and recognizing that the scaling factor is equal to one for this study, Eq. (2.18) is obtained.

$$\frac{\mathrm{d}e_x}{\mathrm{d}\theta} = -\frac{3h^4 \sin(\Omega+\omega)(\frac{p_\odot \rho A}{m})}{2\mu^3} \tag{2.18}$$

Now find the time derivative of e_x in Eq. (2.19) using Eq. (2.18) and the derivative of Eq. (2.1), where e_N is the natural eccentricity. Use the assumption that $h^2 = \mu a(1-e^2) \approx \mu a$ [21, 23].

$$\dot{e}_x = \frac{\mathrm{d}e_x}{\mathrm{d}\theta}\frac{\mathrm{d}\theta}{\mathrm{d}t} = \frac{-3a^2 p_\odot \rho A}{2\mu m}\sin(\Omega+\omega)n = -e_N n_\oplus \sin(\Omega+\omega) \tag{2.19}$$

Note that n is the mean motion of the satellite around the Earth, while $n_\oplus$ is the mean motion of the Earth around the Sun (a.k.a. $\dot{\alpha}$). Since the mean motion is defined as $n^2 = \frac{\mu}{a^3}$ [21, 23], Eq. (2.20) defines the natural eccentricity.

$$e_N = \frac{3p_\odot \rho A}{2mn_\oplus na} \tag{2.20}$$

When the data from a generic Eurostar 2000 satellite is plugged in, this value is similar to the results of the operators who proposed the new disposal orbit [13]. Also note that when integrated, e_x matches Eq. (2.1). This eccentricity component helps the eccentricity vector trace a full circle for $\alpha = \Omega + \omega = 0$ to 2π radians as expected [12]. This also matches the behavior described in the Eurostar 2000 literature [13].

When the orbit's perigee is aligned with the Sun, the orbit becomes sun-synchronous-like. It maintains its orientation with respect to the Sun, but the argument of periapsis changes instead of the right ascension of the ascending node (which remains constant) [21]. This is mainly an argument of semantics due to the small eccentricity of this orbit.

2.3 Derivation of Ideal $\dot{e}_y$

A similar analysis is conducted for e_y. Using Eq. (2.1), the derivative of e_y is approximated in a similar fashion. Start with Eq. (2.21).

$$\delta e_y = \int_0^T \Big(\dot{e} \sin(\Omega + \omega) + e(\dot{\Omega} + \dot{\omega}) \cos(\Omega + \omega) \Big) \tag{2.21}$$

Substitute Eq. (2.3) into Eq. (2.21) to get Eq. (2.22).

$$\delta e_y = \sin(\Omega + \omega) \int_0^T \dot{e} \mathrm{d}t + \frac{h \cos(\Omega + \omega) a_\odot}{\mu} \int_0^T \left(1 + \frac{\sin^2 \theta}{1 + e \cos\theta} \right) \mathrm{d}t \tag{2.22}$$

With the results from the previous analysis for e_x, Eq. (2.22) becomes Eq. (2.23) [20].

$$\delta e_y = \frac{3\pi h^4 \cos(\Omega + \omega) a_\odot}{\mu^3} \tag{2.23}$$

The derivative of e_y with respect to θ over one orbit is approximated in Eq. (2.24).

$$\frac{\mathrm{d}e_y}{\mathrm{d}\theta} = \frac{\delta e_y}{2\pi} = \frac{3h^4 \cos(\Omega + \omega) a_\odot}{2\mu^3} \tag{2.24}$$

Now find the time derivative of e_y in Eq. (2.25) using the same procedure as $\dot{e}_x$.

$$\dot{e}_y = \frac{\mathrm{d}e_y}{\mathrm{d}\theta} \frac{\mathrm{d}\theta}{\mathrm{d}t} = \frac{3a^2 p_\odot \rho A}{2\mu m} \cos(\Omega + \omega) n = e_N n_\oplus \cos(\Omega + \omega) \tag{2.25}$$

The natural eccentricity is again Eq. (2.20). Note that when integrated, e_y matches Eq. (2.1) and therefore creates the expected eccentricity circle with e_x [12].

2.4 Effect on Radius of Periapsis

Now that the eccentricity behavior is derived, the corresponding change in the radius of periapsis (r_p), defined in Eq. (2.26), can be examined.

$$r_p = a(1 - e) \tag{2.26}$$

Start with the Gaussian variational equation for the semi-major axis in Eq. (2.27) [23].

$$\dot{a} = \frac{2a^2}{h} \left(e \sin\theta a_r + (1 + e\cos\theta) a_\theta \right) \tag{2.27}$$

With the current definitions for the accelerations, Eq. (2.27) simplifies to Eq. (2.28).

$$\dot{a} = \frac{2a^2 a_\odot}{h}(-e\sin\theta\cos\theta + \sin\theta + e\sin\theta\cos\theta) = \frac{2a^2 a_\odot}{h}\sin\theta \tag{2.28}$$

Now solve for the semi-major axis change over one orbit of the satellite around the Earth. Start with Eq. (2.29).

$$\delta a = \int_0^T \frac{2a^2 a_\odot}{h}\sin\theta \mathrm{d}t \tag{2.29}$$

Change the integration variable from time to true anomaly in the same manner as before to get Eq. (2.30).

$$\delta a = \frac{2h^2 a^2 a_\odot}{\mu^2}\int_0^{2\pi} \sin\theta(1 - 2e\cos\theta)\mathrm{d}\theta \tag{2.30}$$

Using the assumption that $h^2 = \mu a$, Eq. (2.30) is equivalent to Eq. (2.31), which is solved to get Eq. (2.32) [20].

$$\delta a = \frac{2a^3 a_\odot}{\mu}\left(\int_0^{2\pi}\sin\theta\mathrm{d}\theta - 2e\int_0^{2\pi}\sin\theta\cos\theta\mathrm{d}\theta\right) \tag{2.31}$$

$$\delta a = \frac{2a^3 a_\odot}{\mu}\left(-\cos\theta|_0^{2\pi} - 2e\left(\frac{\sin^2\theta}{2}\right)|_0^{2\pi}\right) = 0 \tag{2.32}$$

Therefore the semi-major axis does not change over one orbit around the Earth, and by extension remains constant for this analysis. This intuitively makes sense for the period of the orbit to remain constant (an assumption that is not violated greatly by the solar radiation pressure perturbation) [23]. This is also dependent on the assumption that the satellite is always in sunlight, which allows the changes accrued over one satellite orbit to cancel each other out [11, 21]. (Even with eclipses, the change in semi-major axis at GEO is shown in the very small - sometimes less than a meter over the entire year [11].) Therefore the only change in the radius of periapsis, defined in Eq. (2.26), over the year is due to the changing eccentricity values [21, 23]. By using the maximum eccentricity value, the minimum radius of periapsis achieved over the year can be calculated.

As an example, the traditional and proposed orbits are compared for a Eurostar 2000 satellite. The average solar pressure ($p_\odot$) is taken as 4.57 x 10^{-6} N/m^2 [21] and the Eurostar 2000 satellite's ballistic radiation coefficient (BC) is 0.05 m^2/kg [4]. Note that the numerical value for the GEO semi-major axis changes depending on how many perturbations are included in its calculation. For

this study, the GEO semi-major axis is 42165.8 km. This is taken from Lagrangian calculations where the latitude variation and the long-term drift due to the Sun and the Moon are nulled [12].

The traditional semi-major axis for the Eurostar 2000 satellite is 42,450.800 km, while the proposed semi-major axis is 42,424.407 km. The traditional orbit raises the radius of periapsis and semi-major axis 285.000 km, while the proposed orbit raises the radius of periapsis 235.000 km and the semi-major axis 258.607 km. These results match the findings in literature [4].

2.5 Fuel Savings

The change in the semi-major axis between the two disposal orbits reduces the fuel needed to reorbit, which is one of the drivers of this research. While multi-year orbit evolution is not addressed in this study, the proposed orbit is a short term solution to help keep these satellites above the GEO belt longer if not enough fuel is allocated for reorbiting. Again, a generic Eurostar 2000 satellite is used as an example. There are many types of maneuvers that can reorbit a GEO satellite into the proper SSO. For ease of comparison, a standardized transfer is used to compare the traditional reorbit fuel costs to the proposed reorbit fuel costs. Two maneuvers are used: one to raise the apoapsis of the transfer orbit and one to make it the perigee of the new orbit [21, 23]. The equations for both reorbit methods are the same.

Using the assumption that the GEO orbit is circular, the ΔV for the first maneuver is calculated in Eq. (2.33) using Eq. (2.34) [21, 23].

$$\Delta V_1 = \sqrt{\frac{2\mu}{a_{\text{GEO}}} - \frac{\mu}{a_{\text{Trans}}}} - \sqrt{\frac{\mu}{a_{\text{GEO}}}} \tag{2.33}$$

$$a_{\text{Trans}} = \frac{a_{\text{GEO}} + a_{\text{SSO}}}{2} \tag{2.34}$$

Similarly, the second ΔV is calculated in Eq. (2.35) [21, 23].

$$\Delta V_2 = \sqrt{\frac{2\mu}{R_{p,SSO}} - \frac{\mu}{a_{\text{SSO}}}} - \sqrt{\frac{2\mu}{R_{p,SSO}} - \frac{\mu}{a_{\text{Trans}}}} \tag{2.35}$$

The difference between the traditional and proposed orbits lies in the a_{SSO} term. For the traditional orbit, this is the new radius of periapsis. However, this radius of periapsis must include

the solar radiation pressure term, and is therefore higher than the proposed method's radius of periapsis.

For the new method, a_{SSO} is calculated using Eq. (2.26) and the natural eccentricity. However, calculating this is complicated since the semi-major axis of the new disposal orbit is included in the natural eccentricity calculation. Therefore start with Eq. (2.20) and substitute Eq. (2.26) to get Eq. (2.36).

$$e_N = \frac{3p_\odot \rho A}{2mn_\oplus n r_p}(1 - e_N) = \beta(1 - e_N) \tag{2.36}$$

This is rearranged by Eq. (2.37) to get Eq. (2.38).

$$(1 + \beta)e_N = \beta \tag{2.37}$$

$$e_N = \frac{\beta}{1 + \beta} = \frac{\frac{3p_\odot \rho A}{2mn_\oplus n r_p}}{1 + \frac{3p_\odot \rho A}{2mn_\oplus n r_p}} \tag{2.38}$$

This eccentricity is used to calculate the necessary a_{SSO} to get the second ΔV. The total ΔV is then compared between the two methods.

To give scope to the amounts of fuel being discussed, an average GEO reorbit fuel requirement is 11 m/s for IADC recommendations (2.3% of the average station-keeping fuel for 10 years) [8]. In particular, reorbiting a Eurostar 2000 satellite (natural eccentricity = 0.00055645) with the traditional method costs 10.338 m/s for 285 km increase, while the proposed method only costs 9.383 m/s. This might seem insignificant, but 0.956 m/s of fuel can extend the mission of an uncontrolled satellite for many months [4] or leave extra margin for reorbiting. It also helps avoid uncertainty for the behavior of the last bit of fuel, which is difficult to measure and can perform randomly due to bubbling, etc [8, 13]. In addition, these results match the results of the operators who proposed this new disposal orbit [4].

Chapter 3

Ideal Proposed Orbit Simulations

Now that the proposed orbit has been proven mathematically to achieve the desired eccentricity behavior, it is simulated in two forms. The first is a MATLAB simulation, which is based directly on the derivation results. This is intended to show these results in a more intuitive form, as well as verify them by matching results in published literature. The second is a series of simulations for NASA's open source General Mission Analysis Tool (GMAT). This is used to simulate the behavior under multiple influences (gravitational perturbations, third-body effects, and solar radiation pressure). GMAT 2011a was used for this study, which uses the same model for the solar radiation pressure force as shown in Eq. (1.2) [1].

3.1 MATLAB Simulation

For the first simulation, the proposed orbit is modeled in MATLAB. The results are listed in Table 3.1, where the ratios are taken with respect to the idealized natural eccentricity and the factors compare the actual components to the idealized components. For example, the center X ratio is the ratio of the eccentricity circle center's X coordinate to the ideal natural eccentricity (i.e. the circle's radius). Most of these values are listed for comparison with later results. Note that in Fig. 3.1 the eccentricity vector starts on the e_x axis and traces a circle. Since the circle is based on the origin of the eccentricity plane, the length of the eccentricity vector, and therefore the eccentricity magnitude, remains the same. Since the eccentricity magnitude remains constant, the initial eccentricity magnitude is the maximum eccentricity magnitude. This gives the constant

Table 3.1: Proposed Orbit Eccentricity Summary

Numerator Factor	1
Denominator Factor	1
Perigee Error	0°
Initial e_x	0.00055645
Initial e_y	0
Initial $\|e\|$	0.00055645
Maximum $\|e\|$	0.00055645
Initial Eccentricity Ratio	1
Center X Ratio	0
Center Y Ratio	0

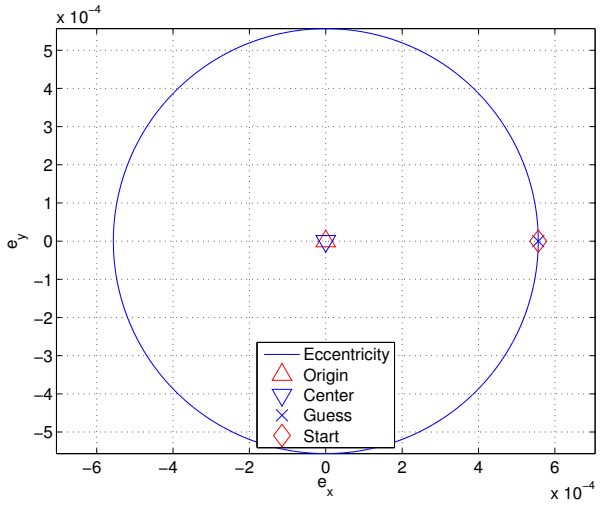

Figure 3.1: Proposed Orbit Eccentricity Vector Behavior Over One Year

radius of periapsis in Fig. 3.2.

Note that while the initial right ascension of the Sun is assumed to be 0°, this behavior occurs no matter what the right ascension is as long as the orbit's perigee points toward the Sun. The eccentricity vector simply starts tracing the circle at a different point on the circle.

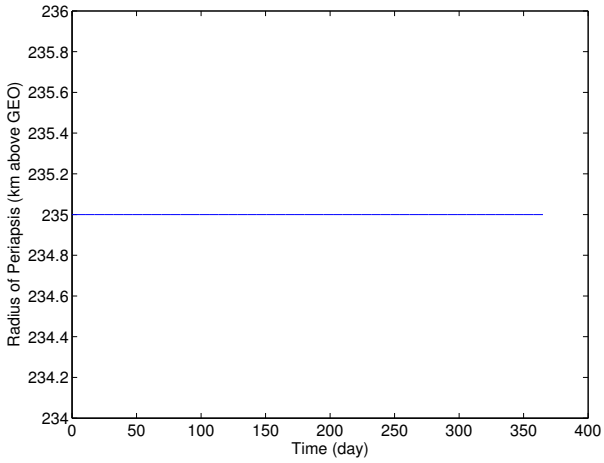

Figure 3.2: Proposed Orbit Radius of Periapsis

3.2 GMAT Simulations

For the second simulation, both the traditional and proposed orbits are modeled in GMAT for more realistic results.

3.2.1 Traditional Disposal Orbit

For comparison, the GMAT simulation models the evolution of a traditional circular disposal orbit and the proposed disposal orbit over one year. The inputs for the traditional disposal orbit analysis are shown in Table 3.2. A generic Eurostar 2000 satellite is used, so the satellite parameters are either average values (referenced) or calculated (c) to achieve a ballistic radiation coefficient (BC) of 0.05 [4]. Otherwise, these are the default GMAT values. Simulation conditions such as the gravity model, etc., are also listed. The eccentricity behavior for this traditional orbit is shown in Fig. 3.3(a). Note that the eccentricity increases from zero, so the radius of periapsis will decrease.

3.2.2 Proposed Disposal Orbit

The proposed orbit has two adjustments to the traditional orbit. The first is to target the natural eccentricity instead of a null eccentricity. By using Eq. (2.20) and the given information,

Table 3.2: Initial GMAT Parameters

Parameter	*Value*
Epoch	21545 TAI Modified Julian Date
Coordinate System	Earth MJ2000 Equatorial
Semi-major Axis	42,450.8000 km (c)
Eccentricity	1 x 10^{-15} (c)
rest of Kep. elements	0°
Initial Quaternion	0,0,0,1
Initial Attitude Rate	0°/s
Dry Mass	1500 kg [22]
Reflectivity	1.5 [23]
Area for Solar Radiation Pressure	50 m^2 (c)
Burns	none
Integrator	RungeKutta89
Initial Step Size	60 s
Accuracy	1 x 10^{-11}
Minimum Step Size	0.001 s
Maximum Step Size	2700 s
Maximum Step Attempts	2,147,483,647
Force Model Error Control	Root Sum Square Step
Force Model Central Body	Earth
Primary Body	Earth
Gravity	Joint Gravity Model-2 Degree 8 Order 8
Drag	None
Solar Radiation Pressure	checked "on"
Propagate Mode	None
Stop Tolerance	1 x $10^{-}7$
Stopping Conditions	365.2421897 days [21]

the natural eccentricity for the simulated Eurostar 2000 satellite is calculated as 5.5644595 x 10^{-4}. Research has shown that satellites are capable of obtaining eccentricities of 5 x 10^{-4} or less [3]. Note that this is also similar to the targeted eccentricity from the literature studies of the Eurostar 2000 satellite, which from $e_N = 0.0115\rho A/m$ is calculated at 5.75 x 10^{-4}[4]. The second adjustment is pointing the orbit's perigee toward the Sun. This is accomplished in GMAT by starting the simulation at a vernal equinox and setting Ω, ω, and θ to zero. Vernal equinox is set as 5:14 March 20, 2012, Universal Time [16]. Note that the eccentricity results in Fig. 3.3(b) do not vary nearly as much as in Fig. 3.3(a).

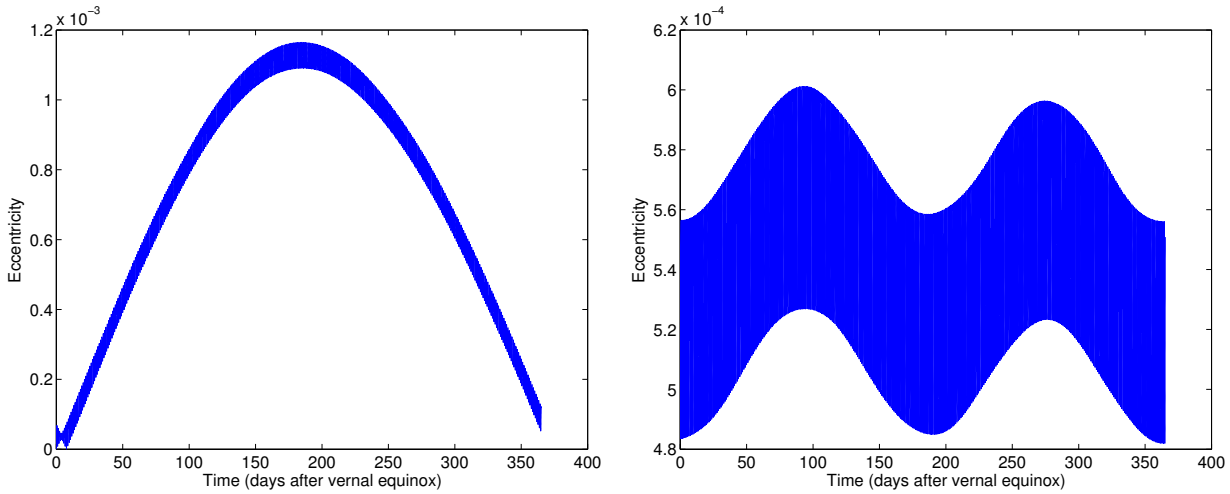

(a) Traditional Orbit (b) Proposed Orbit

Figure 3.3: Eccentricity Magnitude Comparison

3.2.3 Radius of Periapsis Comparison

The radius of periapsis trends for the two orbits are the opposite of the eccentricity trends, as indicated in Eq. (2.26). (The radius of periapsis does include some extra perturbations from the semi-major axis that are not due to solar radiation pressure.) The radius of periapsis differences between the traditional disposal orbit and the proposed orbit are demonstrated in Fig. 3.4(a) and Fig. 3.4(b). For the traditional orbit, the radius of periapsis decreases about 50 km from its initial value, while the proposed orbit varies much less. Third body perturbations have not yet been added, so this is the lower limit within IADC boundaries. (The Earth's gravity model causes the radius of periapsis to dip into the 35 km allocated to gravitational and third-body effects.)

While the expected trends from the derivation and MATLAB simulations are evident, there are other trends as well. This is expected since these simulations include many other factors than just solar radiation pressure. Gravitational perturbations from the Earth, eclipses, and out-of-plane effects are included above. This behavior is further discussed in Appendix A. However, one major contributor that has not yet been simulated is third-body perturbations, addressed in the next section.

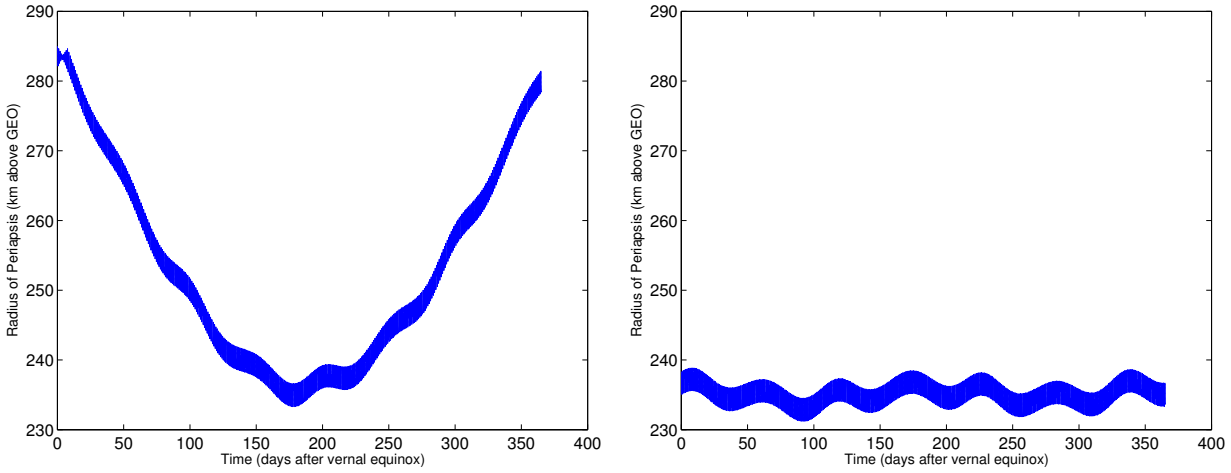

(a) Traditional Orbit

(b) Proposed Orbit

Figure 3.4: Radius of Periapsis over One Year

3.2.4 Third Body Perturbations

The other significant effect at GEO is third body perturbations from the Sun and the Moon. Analytically examining this effect is beyond the scope of this thesis, but the previous GMAT simulations are now repeated with third body perturbations added to show that despite third-body perturbations, the overall effect on the radius of periapsis is the same. Eccentricity results are shown in Fig. 3.5(a) for the traditional orbit and Fig. 3.5(b) for the proposed orbit. These perturbations are more frequent and random than the gravity perturbations, but they are also much smaller (described further in Appendix A). The mitigation between Fig. 3.6(a) and Fig. 3.6(b) still occurs. Note that the radius of periapsis now varies over twice the distance as in Fig. 3.4(b), but the orbit still does not enter the 200 km GEO protected zone.

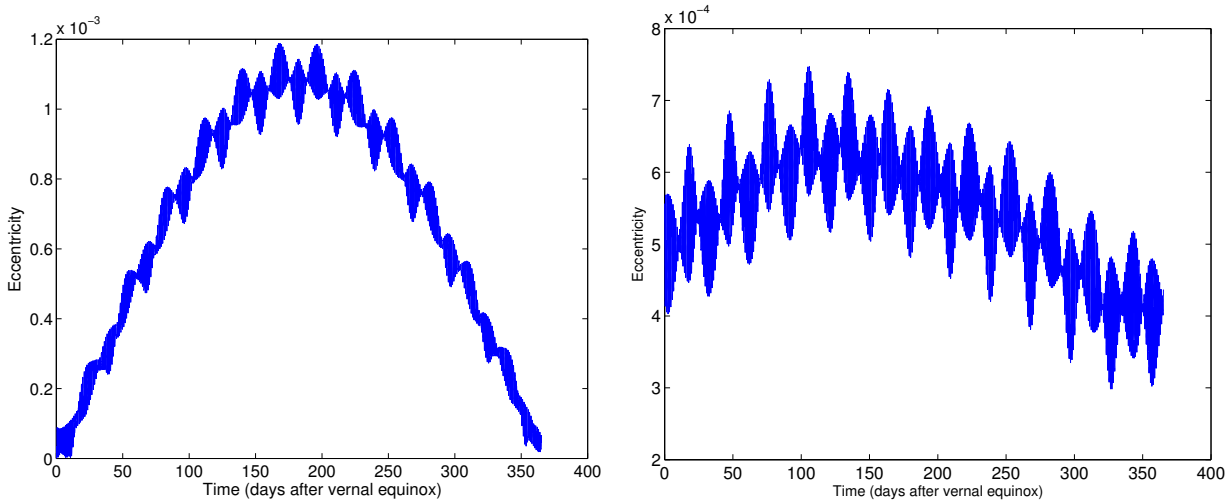

(a) Traditional Orbit (b) Proposed Orbit

Figure 3.5: Eccentricity Magnitude with Third Body Effects over One Year

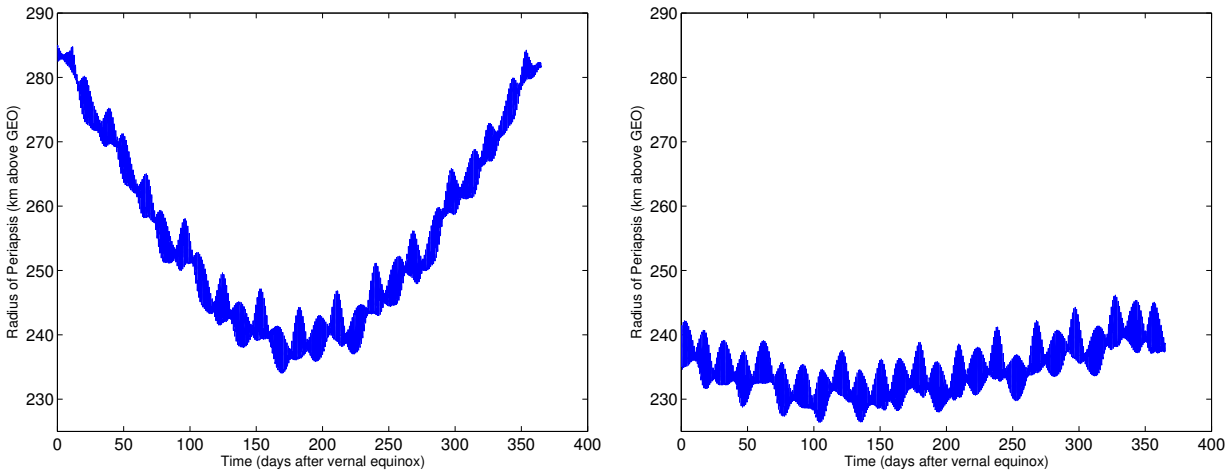

(a) Traditional Orbit (b) Proposed Orbit

Figure 3.6: Radius of Periapsis with Third Body Effects over One Year

Chapter 4

Sensitivity to Eccentricity

This eccentricity vector modification is intriguing and has merit for reorbit applications, but the previous analysis is for the idealized case. Just as important is how this modification is affected when errors in satellite knowledge or initialization occur. This modification is not useful if the proper initial conditions are almost impossible to obtain. The effects of the major natural eccentricity error sources and eccentricity initialization errors are explained in this chapter, and the effects of a perigee pointing error are discussed in Chapter 5.

4.1 Natural Eccentricity Errors

For clarity, the natural eccentricity is repeated in Eq. (4.1). Numerous errors can be introduced in this calculation due to the inexact nature of spacecraft management. Note that the spacecraft knowledge errors in Eq. (4.1) are the same as the parameters of solar acceleration in Eq. (1.2).

$$e_N = \frac{3p_{\odot}\rho A}{2mn_{\oplus}na} \tag{4.1}$$

At first, the initial eccentricity is assumed to be set by the guessed values to isolate the spacecraft knowledge errors. In other words, the initial eccentricity is set exactly (an assumption that will be disregarded later in this chapter). Therefore the center of the eccentricity circle, and the overall eccentricity behavior, is developed from both the guessed (g) and the real (R) initial conditions. This is most easily shown by examining the center of the eccentricity circle. The coordinates of the center are shown in Eq. (4.2) [12]. Remember that the orbit's perigee is assumed

to be pointing directly toward the Sun, so $\alpha = \Omega + \omega$.

$$\begin{aligned} X &= e_{x,0} + e_{N,\mathrm{R}} \cos(\alpha_0 - \pi) = e_{N,\mathrm{g}} \cos(\Omega_0 + \omega_0) - e_{N,\mathrm{R}} \cos\alpha_0 \\ &= (e_{N,\mathrm{g}} - e_{N,\mathrm{R}}) \cos(\Omega_0 + \omega_0) \\ Y &= e_{y,0} + e_{N,\mathrm{R}} \sin(\alpha_0 - \pi) = (e_{N,\mathrm{g}} - e_{N,\mathrm{R}}) \sin(\Omega_0 + \omega_0) \end{aligned} \tag{4.2}$$

4.1.1 Numerator Errors

Multiple components of the natural eccentricity's numerator are susceptible to errors. However, Eq. (4.1) shows that the same percentage error in each component results in the same error in the natural eccentricity, regardless of the error magnitude.

4.1.1.1 Numerator Components

The solar radiation pressure ($p_\odot$) is the solar irradiance divided by the speed of light, but its magnitude depends on the stage of the solar cycle [21]. Solar minima and solar maxima directly affect the natural eccentricity, and therefore the radius of periapsis. While analyzing the long-term evolution of solar radiation pressure is beyond the scope of this thesis, the sensitivity of the behavior to changes from the mean solar radiation pressure can be examined.

Reflectivity (ρ) affects how much momentum is transferred by the sunlight [23]. Knowing this parameter accurately is difficult because it varies for different materials and changes over time [21]. A reflectivity of zero indicates a transparent surface, which means no force is transferred. A reflectivity of one means the sunlight is fully absorbed. A reflectivity of two means the sunlight is reflected and the force imparted on the satellite is doubled [21, 23].

To stay within the scope of this thesis, an average cross-sectional area (A) is used. However, variations in area can be examined for their impact on this short-term perturbation. As mentioned p reviously in Chapter 1, this also allows the satellite's attitude to be ignored and a 0° incidence angle to be assumed [21].

4.1.1.2 Single Error Analysis

There are a number of ways to visualize the errors in the eccentricity behavior , but one of the more intuitive is to look at the behavior of the eccentricity vector in the eccentricity plane over one year, shown in Fig. 4.1. Area was selected as the erroneous variable, but each of the previous parameters could be chosen since these results are normalized to percentage values. To simulate this, the actual area is set as 10% greater than it is assumed. The results are summarized in Table 4.1. Note that the eccentricity magnitude increases from the initial set value in Fig. 4.2(a), which will decrease the radius of periapsis in Fig. 4.2(b). Also note that a 10% increase in the natural eccentricity (due to the numerator error) shifts the center X coordinate left by 10% of the ideal natural eccentricity. This makes sense because the circle is larger but the initial eccentricity is the same.

Note that these results include the assumption that the error occurs when the right ascension of the Sun is 0°. If the right ascension of the Sun is not zero, the same behavior occurs in the eccentricity plane, but along the axis of the initial eccentricity instead of the e_x-axis. This is logical because the solar radiation force acts along this axis. When the perigee is aligned exactly, this is the axis of the eccentricity vector. The analyses in the thesis are conducted with the right ascension of the Sun at 0° to clarify patterns in the behavior.

Table 4.1: Numerator Error Eccentricity Summary

Numerator Factor	1.1
Denominator Factor	1
Perigee Error	0°
Initial e_x	0.00055645
Initial e_y	0
Initial $\|e\|$	0.00055645
Maximum $\|e\|$	0.00066774
Initial Eccentricity Ratio	1.1
Center X Ratio	-0.1
Center Y Ratio	0

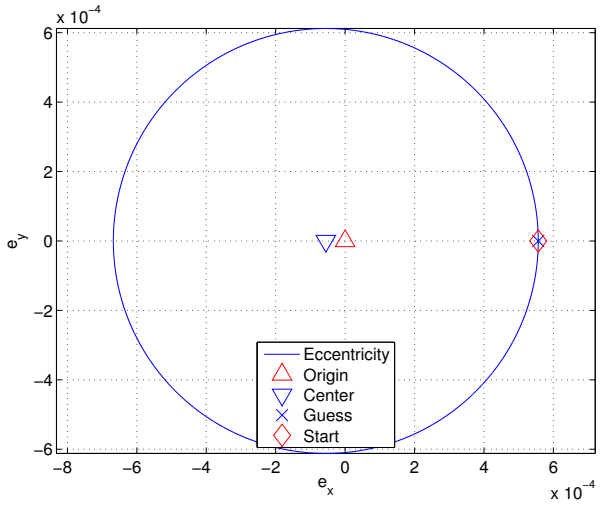

Figure 4.1: Eccentricity Vector Behavior over One Year with a Numerator Error

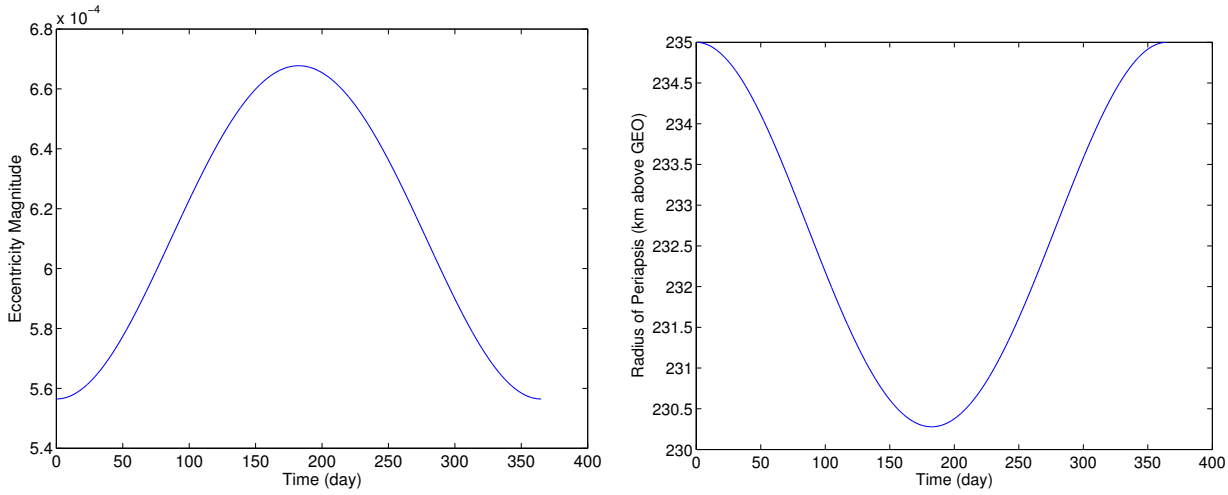

(a) Eccentricity Magnitude

(b) Radius of Periapsis

Figure 4.2: Results from a Numerator Error

4.1.1.3 Monte Carlo Parameters

While single case error analysis lead to intuitive insights, it is one part of the overall determination of sensitivity. Gaussian distributions of the errors are examined to reveal overall trends due to these errors. To accomplish this, the "gmdistribution" command is used to create an object with a Gaussian distribution in MATLAB. This distribution is then sampled to generate raw data for

the analysis. The sample size was determined by finding a distribution that followed the percentage expectations of an ideal Gaussian distribution. This means that 68.26% of the values were within one standard deviation of the mean, 95.44% of the values were within two standard deviations of the mean, and 99.74% of the values were within three standard deviations of the mean [14]. This performance standard also had to be balanced against computing time and power. Therefore 6000 values were run for each Gaussian distribution, which were sorted into 25 bins for the histograms. In five test cases, the sample data averaged 0.328% error for one standard deviation, 0.182% error for two standard deviations, and 0.042% for three standard deviations. Not much improvement was noted for higher values, but computational time was significantly increased.

4.1.1.4 Monte Carlo Analysis

These parameters were used to analyze a Gaussian distribution of numerator errors. Area was again selected as the erroneous variable. A Gaussian distribution was created in MATLAB using 10% of the mean area as the standard deviation. Figure 4.3(a) shows the resulting center X ratios, described by the trendline in Eq. (4.3). The ratio of the area to its mean is AR, which is equivalent to the ratio of the actual natural eccentricity to the ideal (id) natural eccentricity.

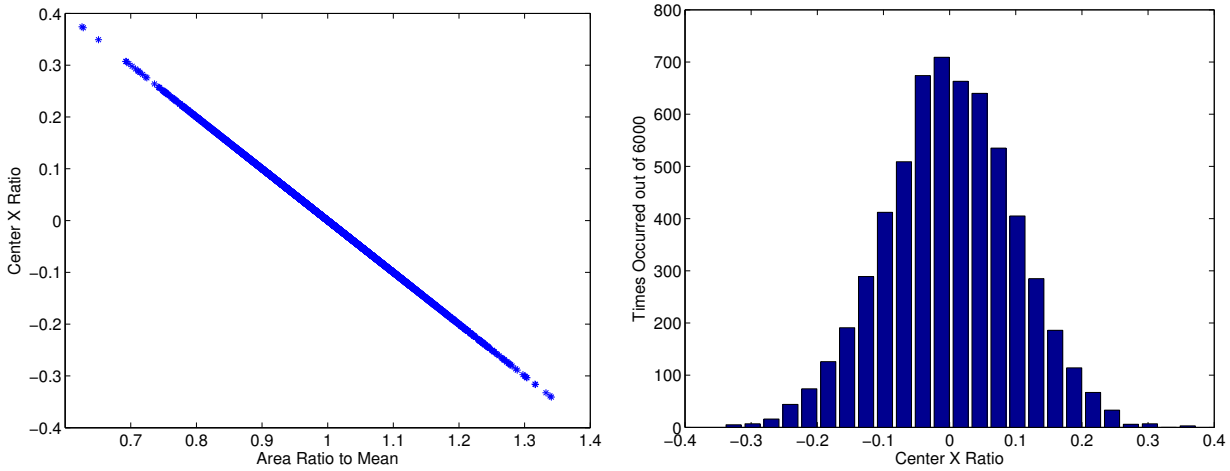

(a) Raw

(b) Histogram

Figure 4.3: Center X Ratio Results from Numerator Errors

There is a linear relationship between the area ratio and the center X ratio. This is intuitive since the numerator errors merely change the radius of the eccentricity circle, which shifts its center in the eccentricity plane accordingly. This linear relationship translates to the histogram of the center X ratio results in Fig. 4.3(b), which also demonstrates a Gaussian distribution similar to the error distribution.

$$\frac{X_c}{e_{N,\text{id}}} = -AR + 1 \tag{4.3}$$

Note that if the components in Eq. (4.3) are rearranged and the natural eccentricity ratio is substituted for AR, Eq. (4.4) occurs. This indicates that the shift in the center X coordinate, which ideally is zero, is the opposite of the difference of the actual natural eccentricity from the ideal natural eccentricity. This was shown in the single error analysis and is expanded here for all numerator errors. Again, since the initial right ascension of the Sun is assumed to be 0°, all the changes occur in the x-axis.

$$X_c = e_{N,\text{id}} - e_N \tag{4.4}$$

Fig. 4.4 shows the maximum eccentricity magnitude obtained for each area ratio. Note that the trendline for the errors in the right side of Fig. 4.4 is shown in Eq. (4.5). This trendline is especially interesting because the coefficient is twice the idealized natural eccentricity and the y-intercept is the idealized natural eccentricity (the parameters of a generic Eurostar 2000 satellite are used). Note that if AR is zero, the ideal natural eccentricity results.

$$|e|_{\max} = 0.0011129AR - 0.00055645 \tag{4.5}$$

One of the most interesting trends in Fig. 4.4 is that half of the numerator errors do not affect the maximum eccentricity, and by extension the minimum radius of periapsis. While not initially intuitive, this is explained visually in Fig. 4.5. Since the initial eccentricity is assumed to be exactly set, the only change is the size of the eccentricity circle (ideally shown with the dashed line). Errors that increase the natural eccentricity, and therefore the eccentricity circle's size, increase the maximum eccentricity as shown by the solid circle. Errors that decrease the natural eccentricity, on the other hand, create a new eccentricity circle (shown in bold) completely contained in the

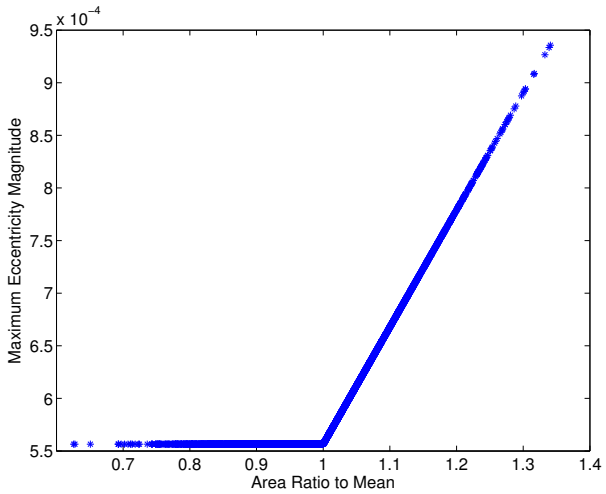

Figure 4.4: Maximum Eccentricity Magnitude from Numerator Errors

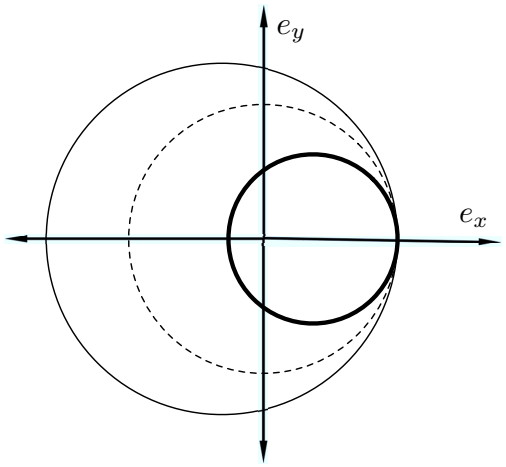

Figure 4.5: Natural Eccentricity Error Explanation

original eccentricity circle. This circle's maximum eccentricity is the initial eccentricity, which is set exactly. Therefore, the maximum eccentricity itself does not change for these errors.

Fig. 4.6(a) shows the minimum radius of periapsis obtained for each area ratio. Note that this behavior opposes the eccentricity behavior due to Eq. (2.26). The trendline for the errors on the right side of Fig. 4.6(a) is shown in Eq. (4.6). A 10% increase in the area decreases the radius of periapsis by 4.7214 km. However, the changed results are still mostly Gaussian as shown in

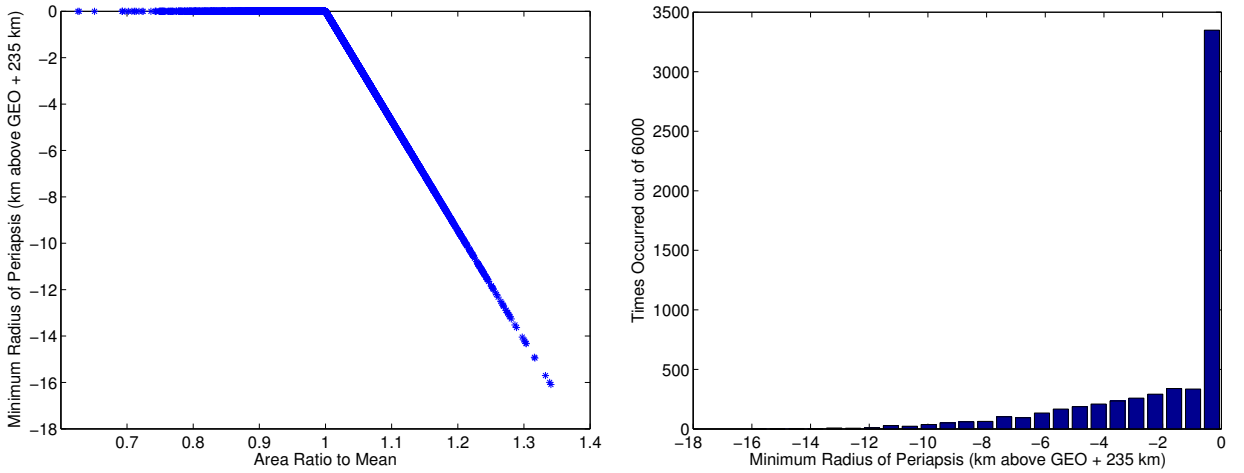

(a) Raw

(b) Histogram

Figure 4.6: Minimum Radius of Periapsis Results from Numerator Errors

Fig. 4.6(b). (Note the "errors" that do not change the radius of periapsis cause the increased value of the right-most column.) These trends are the same for solar radiation pressure and reflectivity. More importantly, this analysis implies that the minimum radius of periapsis can be protected from natural eccentricity errors by targeting the maximum possible natural eccentricity.

$$r_{p\text{min}} = -47.214AR + 47.214 \tag{4.6}$$

4.1.2 Denominator Errors

The main variable susceptible to knowledge errors in the denominator is mass. Denominator error effects are similar numerator error effects because the size of the eccentricity circle is still changed. However, mass is inversely proportional to the natural eccentricity. While the trendlines listed below are much more complicated due to this inverse relationship, the overall effects are the same if the mass error is viewed as an inverted numerator error instead. For example, a 10% increase in mass is comparable to a 10/11% increase in area.

4.1.2.1 Single Error Analysis

To examine the effect of an error in the natural eccentricity's denominator, first look at an individual mass error's effect on the radius of periapsis. For consistency, a 10% error is examined. The results are summarized in Table 4.2. Note that the maximum eccentricity stays the same in this example because increasing the mass decreases the natural eccentricity. As shown in Fig. 4.5, this does not change the maximum eccentricity if the initial eccentricity is assumed exactly set.

Figure 4.7 illustrates that a 10% increased in mass corresponds to a 10/11% decrease in the natural eccentricity and shifts the center X coordinate right 1/11% of the ideal natural eccentricity. Note that the sum of the eccentricity ratio and X ratio is one again. As expected, the eccentricity magnitude decreases from the initial set value in Fig. 4.8(a), which increases the radius of periapsis in Fig. 4.8(b). This same behavior occurs if one of the numerator components is less than expected, just like the numerator increase results are equivalent to a decrease in a denominator component. Once again, the Sun's right ascension is assumed to be 0°.

Table 4.2: Denominator Error Eccentricity Summary

Numerator Factor	1
Denominator Factor	1.1
Perigee Error	0°
Initial e_x	0.00055645
Initial e_y	0
Initial $\|e\|$	0.00055645
Maximum $\|e\|$	0.00055645
Initial Eccentricity Ratio	10/11
Center X Ratio	1/11
Center Y Ratio	0

4.1.2.2 Monte Carlo Analysis

To expand these insights into a general trend of denominator error behavior, analysis was also conducted for a Gaussian distribution of mass errors. The standard deviation is set as 10%

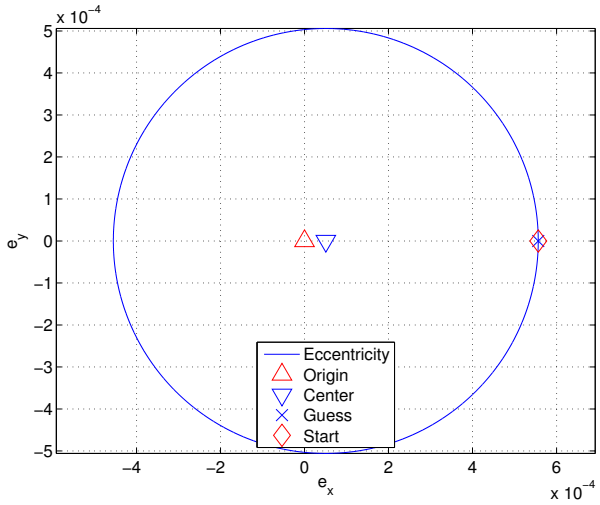

Figure 4.7: Eccentricity Vector Behavior over One Year with a Denominator Error

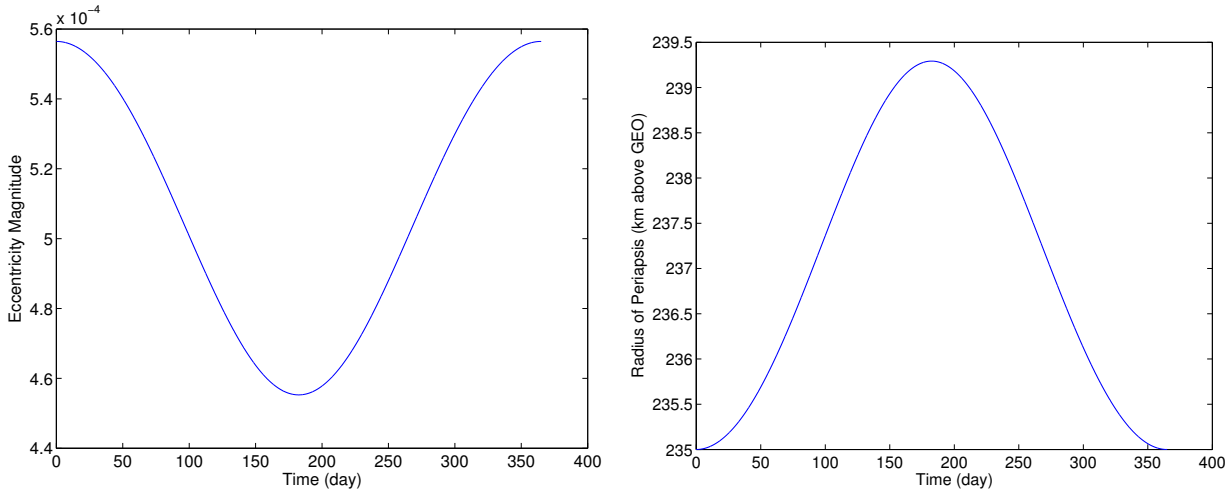

(a) Eccentricity Magnitude

(b) Radius of Periapsis

Figure 4.8: Results from a Denominator Error

of the mean mass. Fig. 4.9(a) shows the center X ratios, which are described by the trendline in Eq. (4.7) (where MR is the mass ratio to its mean). This trendline is more complicated since the mass error corresponds to an inverted numerator error. However the histogram in Fig. 4.9(b) still indicates a Gaussian distribution of results. Again, since the initial right ascension of the Sun is

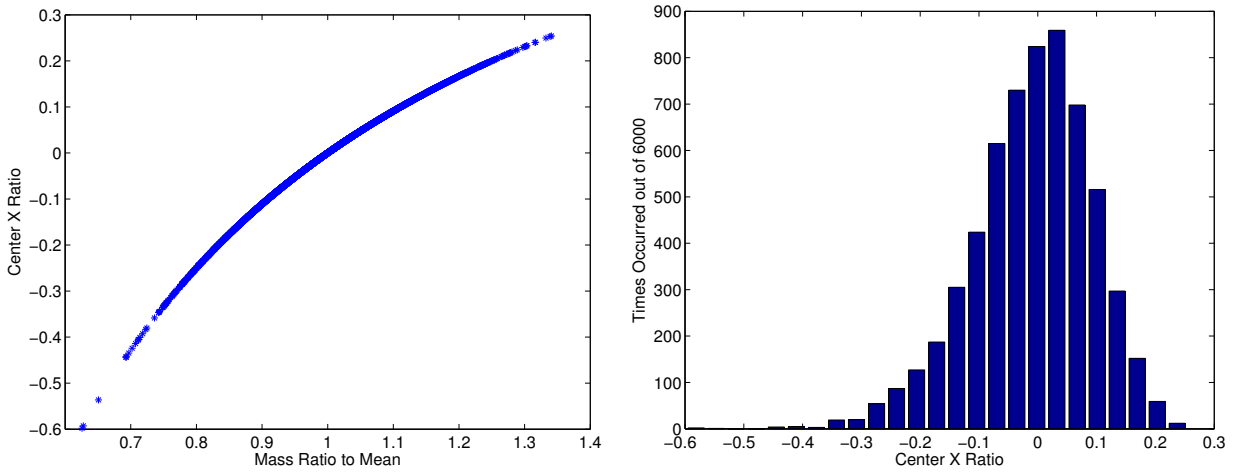

(a) Raw (b) Histogram

Figure 4.9: Center X Ratio Results from Denominator Errors

assumed to be 0°, all the changes occur in the x-axis.

$$\frac{X_c}{e_{N,\text{id}}} = -1.2116MR^4 + 5.9519MR^3 - 11.579MR^2 + 11.147MR - 4.3086 \tag{4.7}$$

Fig. 4.10(a) shows the ratio of the actual natural eccentricity to the ideal natural eccentricity. For mass, this ratio is the inverse of the mass ratio. (This differs from numerator errors, where this ratio was self-defined.) The trendline for the natural eccentricity ratio is shown in Eq. (4.8). Despite the added complexity, the sum of the center X and natural eccentricity ratios is still one as shown in Eq. (4.9), which is equivalent to Eq. (4.3). Again, the histogram in Fig. 4.10(b) indicates a Gaussian distribution of eccentricity ratios.

$$\frac{e_N}{e_{N,\text{id}}} = 1.2116MR^4 - 5.9519MR^3 + 11.579MR^2 - 11.147MR + 5.3086 \tag{4.8}$$

$$\frac{X_c}{e_{N,\text{id}}} + \frac{e_N}{e_{N,\text{id}}} = 1 \tag{4.9}$$

Fig. 4.11 shows the maximum eccentricity magnitude for each mass ratio. The trendline for the errors on the left side of Fig. 4.11 is shown in Eq. (4.10). The non-changing errors are now on the right side of the figure since decreases in mass change the maximum eccentricity.

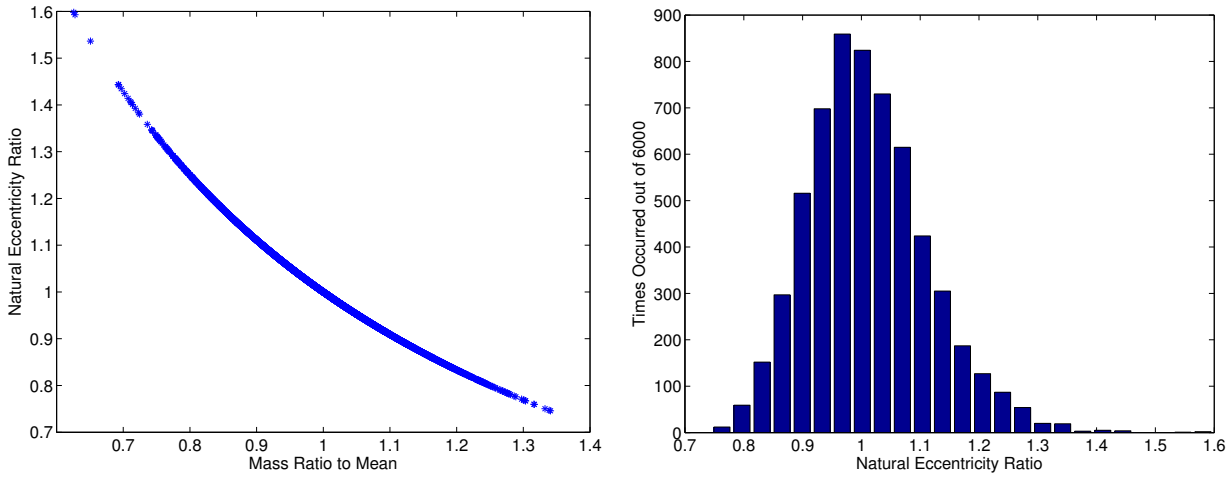

(a) Raw (b) Histogram

Figure 4.10: Natural Eccentricity Ratio Results from Denominator Errors

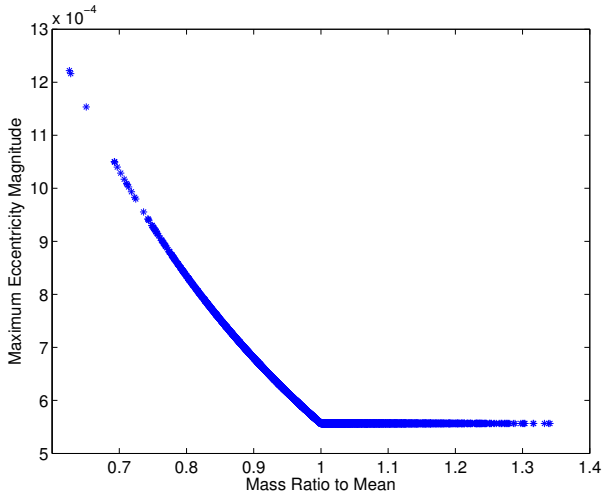

Figure 4.11: Maximum Eccentricity Magnitude from Denominator Errors

$$|e|_{\max} = 0.0028629MR^4 - 0.011984MR^3 + 0.01996MR^2 - 0.016528MR + 0.0062462 \qquad (4.10)$$

Fig. 4.12(a) shows the minimum radius of periapsis for each mass ratio, which again opposes the eccentricity behavior due to Eq. (2.26). The trendline for the errors on the left side of Fig. 4.12(a) is shown in Eq. (4.11). An increase in mass will not affect the minimum radius of periapsis, but a 10% decrease reduces the minimum radius of periapsis by 5.2542 km. However, as shown in

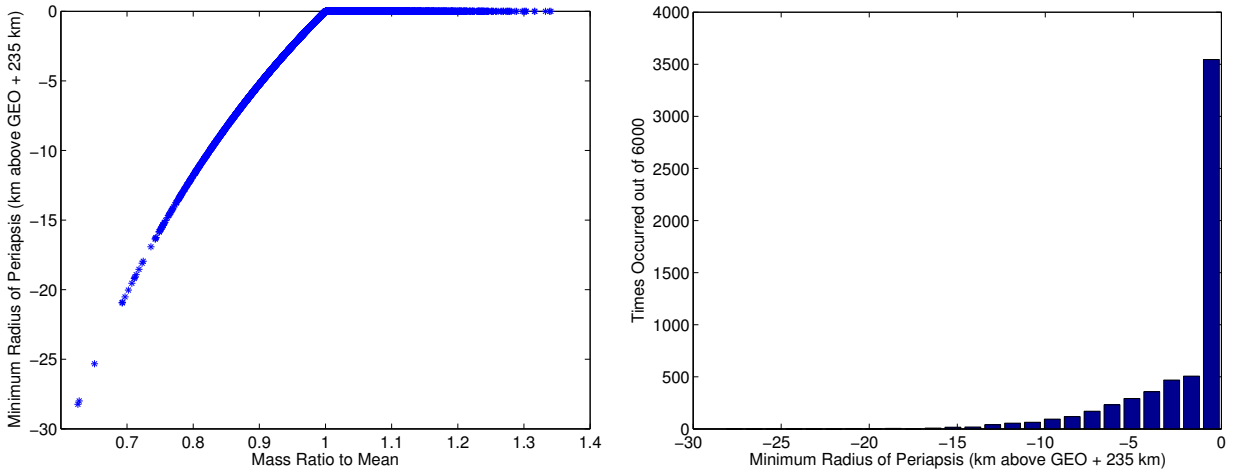

(a) Raw (b) Histogram

Figure 4.12: Minimum Radius of Periapsis Results from Denominator Errors

Fig. 4.12(b), the radius of periapsis results are still Gaussian for the changing values. Once again, the minimum radius of periapsis can be protected from mass errors by using the minimum mass to calculate the maximum possible natural eccentricity.

$$r_{p\min} = -121.46MR^4 + 508.44MR^3 - 846.81MR^2 + 701.21MR - 241.39 \tag{4.11}$$

4.2 Initialization Magnitude Errors

Previously in this chapter, the initial eccentricity is assumed to be set exactly. This section specifically disregards this assumption and examines errors from bad eccentricity magnitude initialization. Here, the natural eccentricity magnitude is known exactly, but the initial eccentricity magnitude is not the same as this known value.

4.2.1 Single Error Analysis

In a similar manner to the natural eccentricity error analysis, first look at an individual initialization error and how it affects the radius of periapsis. Here the achieved eccentricity is 10% greater than the desired (natural) eccentricity. The results are summarized in Table 4.3. Note here that both the initial eccentricity and the maximum eccentricity are bigger than the

natural eccentricity. This is because the initial eccentricity is no longer assumed to be exactly set, therefore it is no longer a fixed point as demonstrated in Fig. 4.13. Even though the eccentricity is maximized at initialization, this still decreases the radius of periapsis, as seen in Fig. 4.14(a) and Fig 4.14(b), because the maximum eccentricity is larger than the natural eccentricity. Note that if the initial eccentricity was smaller than the natural eccentricity, the maximum eccentricity would still increase because the eccentricity circle would be shifted to the left instead of to the right.

Table 4.3: Initialization Error Eccentricity Summary

Numerator Factor	1
Denominator Factor	1.1
Perigee Error	0°
ICerrorFactor	1.1
Initial e_x	0.00061209
Initial e_y	0
Initial $\|e\|$	0.00061209
Maximum $\|e\|$	0.00061209
Initial Eccentricity Ratio	1.1
Center X Ratio	0.1
Center Y Ratio	0

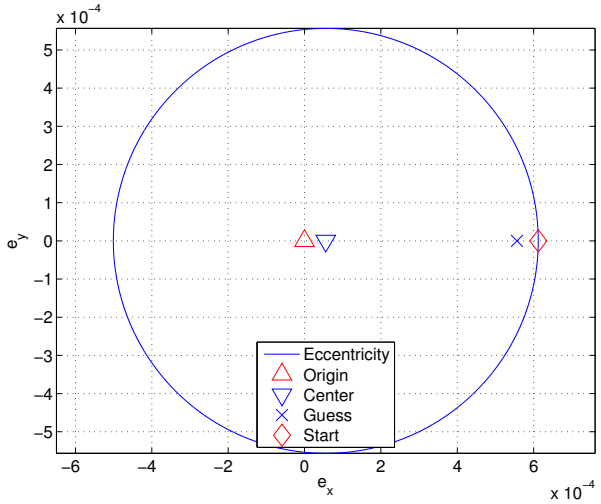

Figure 4.13: Eccentricity Vector Behavior over One Year with an Initialization Error

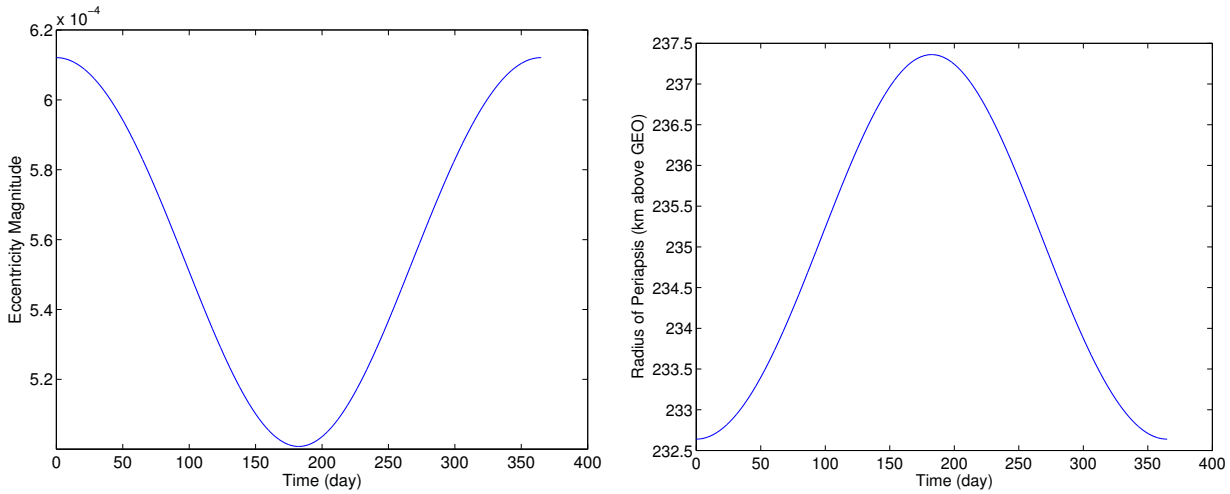

(a) Eccentricity Magnitude

(b) Radius of Periapsis

Figure 4.14: Results from an Initialization Error

Also note that a 10% increased initial eccentricity increases the center X coordinate by 10% of the natural eccentricity. This is the opposite of the numerator errors. This is because an initialization error shifts an eccentricity circle of the same size to a new starting point, whereas numerator errors change the eccentricity circle's size for the same starting point. Again, the right ascension of the Sun is assumed to be 0°.

4.2.2 Monte Carlo Analysis

To expand the single initialization error analysis results to all initialization errors, analysis was conducted for a Gaussian distribution of initialization errors. The distribution uses 10% of the natural eccentricity as the standard deviation. Figure 4.15(a) shows the center X ratios, which are described by the trendline in Eq. (4.12) (where ER is the ratio of the initial eccentricity (e_0) to the natural eccentricity). This trend is also evident in Eq. (4.13), which is formed from Eq. (4.12). Again, the linear relationship between the center X ratio and the eccentricity ratio is intuitive since these errors merely shift the eccentricity circle. This linear relationship translates to the histogram of the center X ratio results in Fig. 4.15(b), which demonstrates a Gaussian distribution similar to

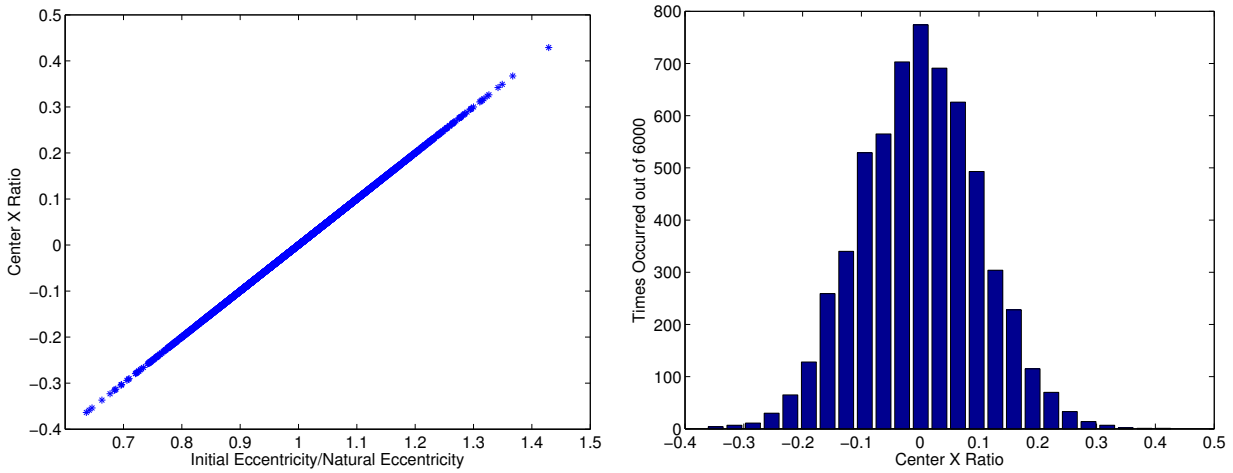

(a) Raw (b) Histogram

Figure 4.15: Center X Ratio Results from Initialization Errors

the error distribution.

$$\frac{X_c}{e_N} = ER - 1 \tag{4.12}$$

$$X_c = e_0 - e_N \tag{4.13}$$

Figure 4.16 shows the maximum eccentricity magnitude obtained for each area ratio. Note that since the initial eccentricity is no longer set as a fixed point, all of the errors now increase the maximum eccentricity. The trendlines for the left and right sides are shown in Eq. (4.14). As expected, these expressions reflect symmetric behavior since shifting the eccentricity circle right or left in the eccentricity plane results in the same maximum eccentricity change. Note that the ER coefficients are the natural eccentricity and the left y-intercept is twice the idealized natural eccentricity, so an ER of one results in the maximum eccentricity equaling the natural eccentricity as expected.

$$\begin{aligned} |e|_{\text{max,left}} &= -0.00055645ER + 0.0011129 \\ |e|_{\text{max,right}} &= 0.00055645ER \end{aligned} \tag{4.14}$$

Fig. 4.17(a) shows the minimum radius of periapsis obtained for each eccentricity ratio. The trendlines for the left and right sides are shown in Eq. (4.15). As expected, these trendlines

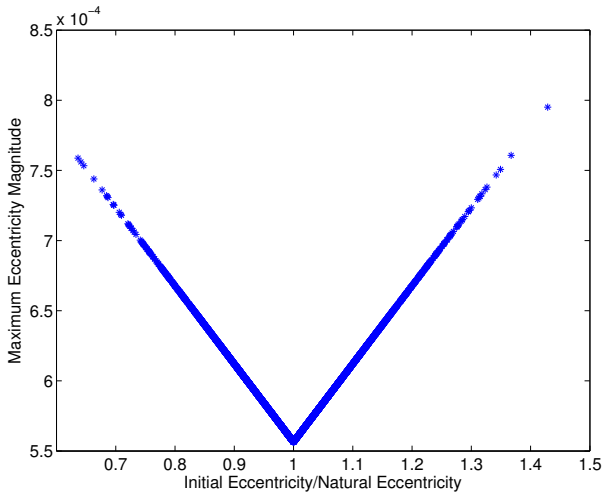

Figure 4.16: Maximum Eccentricity Magnitude from Initialization Errors

oppose the symmetric eccentricity behavior. Note that both a 10% increase and a 10% decrease initialization error decreases the radius of periapsis by 2.3607 km. Interestingly, this is half of the radius of periapsis reduction caused by a 10% increase in the natural eccentricity. This is because while both errors shift the eccentricity circle by the same magnitude (in opposite directions), the natural eccentricity error does so by increasing the eccentricity circle's radius. This change affects the maximum eccentricity vector twice. Since initialization errors act symmetrically on the radius of periapsis, the results represent half a Gaussian distribution as shown in Fig. 4.17(b).

$$\begin{aligned} r_{p\text{min,left}} &= 23.607ER - 23.607 \\ r_{p\text{min,right}} &= -23.607ER + 23.607 \end{aligned} \tag{4.15}$$

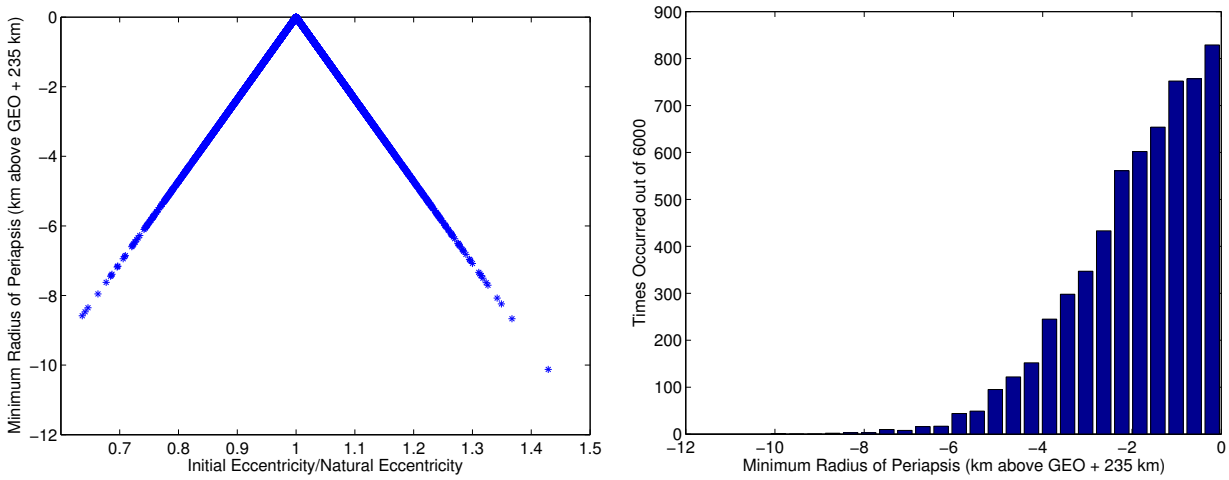

(a) Raw

(b) Histogram

Figure 4.17: Minimum Radius of Periapsis Results from Initialization Errors

Chapter 5

Sensitivity to Perigee Direction

Just as the previous chapter examined various eccentricity errors and their effect on the proposed orbit, this chapter analyzes the effects of perigee offset errors (when the perigee is not pointing directly toward the Sun). To examine this mathematically, add an offset angle ϕ between the Sun direction and perigee as shown in Fig. 5.1. Now $a_r = -a_\odot \cos(\theta + \phi)$ and $a_\theta = a_\odot \sin(\theta + \phi)$, which are expanded into Eq. (5.1). Note that a_h is still zero.

$$\begin{aligned} a_r &= a_\odot(-\cos\theta\cos\phi + \sin\theta\sin\phi) \\ a_\theta &= a_\odot(\sin\theta\cos\phi + \cos\theta\sin\phi) \end{aligned} \tag{5.1}$$

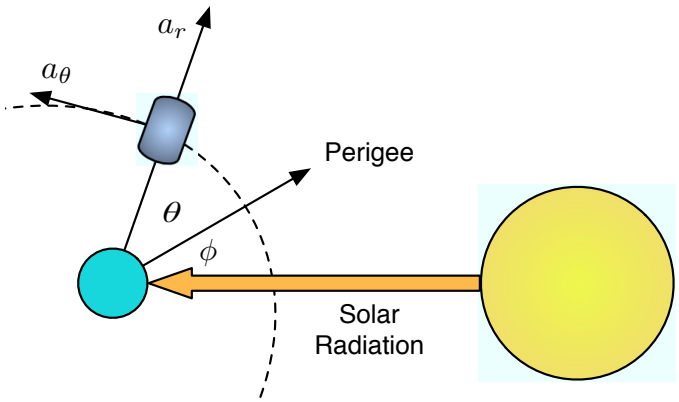

Figure 5.1: General Solar Pressure Force

With this offset error in the perigee direction, the angles are now related by Eq. (5.2),where g is the guess or assumed value, and R is the real or true value.

$$\Omega + \omega = \alpha_{\mathrm{g}} = \alpha_{\mathrm{R}} + \phi \tag{5.2}$$

The true right ascension of the Sun, which determines the behavior of the eccentricity circle, is shown in Eq. (5.3).

$$\alpha_{\mathrm{R}} = \Omega + \omega - \phi \tag{5.3}$$

To isolate the perigee offset error the initial eccentricity magnitude is assumed to be exactly set as the natural eccentricity, so the overall eccentricity vector behavior is developed from both the guessed and real initial conditions.

5.1 Derivation with Perigee Offset

To analyze a perigee offset error's effect mathematically, the modified accelerations are inserted into the Gaussian equations from Eq. (2.2) to get Eq. (5.4).

$$\begin{aligned}
\dot{e} &= \frac{ha_{\odot}}{\mu}\left(\sin\phi + \left(\frac{e+\cos\theta}{1+e\cos\theta}\right)(\sin\theta\cos\phi + \cos\theta\sin\phi)\right) \\
\dot{\omega} &= \frac{ha_{\odot}}{e\mu}\left(\cos\phi + \left(\frac{1}{1+e\cos\theta}\right)(\sin^2\theta\cos\phi + \sin\theta\cos\theta\sin\phi)\right) \\
\dot{\Omega} &= 0
\end{aligned} \tag{5.4}$$

5.1.1 Derivation of $\dot{e}_x$ with Perigee Offset

The approach to this analysis is similar to the approach taken in Chapter 2. To find δe_x, plug Eq. (5.4) into Eq. (2.4) to get Eq. (5.5). Remember that eccentricity is taken to the first order since it is very small.

$$\begin{aligned}
\delta e_x = {} & \frac{ha_{\odot}}{\mu}(\cos(\Omega+\omega)\int_0^T\left(\sin\phi + \frac{e+\cos\theta}{1+e\cos\theta}(\sin\theta\cos\phi + \cos\theta\sin\phi)\right)\mathrm{d}t \\
& - \sin(\Omega+\omega)\int_0^T\left(\cos\phi + \frac{\sin^2\theta\cos\phi + \sin\theta\cos\theta\sin\phi}{1+e\cos\theta}\right)\mathrm{d}t)
\end{aligned} \tag{5.5}$$

Note that when compared to the ideally aligned case, Eq. (5.5) is rewritten as Eq. (5.6), where *id* stands for the ideal perigee-pointing case.

$$\begin{aligned}\delta e_x &= \cos\phi\delta e_{x,\mathrm{id}} + \sin\phi\frac{ha_\odot}{\mu}(\cos(\Omega+\omega)\int_0^T\left(1+\frac{e+\cos\theta}{1+e\cos\theta}\cos\theta\right)\mathrm{d}t \\ &\quad -\sin(\Omega+\omega)\int_0^T\frac{\sin\theta\cos\theta}{1+e\cos\theta}\mathrm{d}t)\end{aligned} \tag{5.6}$$

The perigee offset is assumed constant since one day is relatively small compared to one year. The first term is the effect due to the perigee-aligned solar radiation pressure acceleration component, and the second part is due to the unaligned acceleration component. Continue the derivation by expanding Eq. (5.6) to Eq. (5.7).

$$\begin{aligned}\delta e_x &= \cos\phi\delta e_{x,\mathrm{id}} + \sin\phi\frac{ha_\odot}{\mu}(\cos(\Omega+\omega)\int_0^T(1+(e+\cos\theta)(1-e\cos\theta)\cos\theta)\,\mathrm{d}t \\ &\quad -\sin(\Omega+\omega)\int_0^T(1-e\cos\theta)\sin\theta\cos\theta\mathrm{d}t)\end{aligned} \tag{5.7}$$

Simplify and change the integration variable from time to true anomaly in Eq. (5.8), which is then simplified to Eq. (5.9).

$$\begin{aligned}\delta e_x &= \cos\phi\delta e_{x,\mathrm{id}} + \sin\phi\frac{h^4a_\odot}{\mu^3}(\cos(\Omega+\omega)\int_0^{2\pi}\left(1+\cos^2\theta+e\cos\theta-e\cos^3\theta\right)(1-2e\cos\theta)\,\mathrm{d}\theta \\ &\quad -\sin(\Omega+\omega)\int_0^{2\pi}(1-e\cos\theta)(1-2e\cos\theta)\sin\theta\cos\theta\mathrm{d}\theta)\end{aligned} \tag{5.8}$$

$$\begin{aligned}\delta e_x &= \cos\phi\delta e_{x,\mathrm{id}} \\ &\quad +\sin\phi\frac{h^4a_\odot}{\mu^3}(\cos(\Omega+\omega)\left(\theta|_0^{2\pi}+\int_0^{2\pi}\cos^2\theta\mathrm{d}\theta-e\int_0^{2\pi}\cos\theta\mathrm{d}\theta-3e\int_0^{2\pi}\cos^3\theta\mathrm{d}\theta\right) \\ &\quad -\sin(\Omega+\omega)\left(\int_0^{2\pi}\sin\theta\cos\theta\mathrm{d}\theta-3e\int_0^{2\pi}\sin\theta\cos^2\theta\mathrm{d}\theta\right))\end{aligned} \tag{5.9}$$

Solve Eq. (5.9) to get Eq. (5.10) [20].

$$\begin{aligned}\delta e_x &= \cos\phi\delta e_{x,\mathrm{id}} \\ &\quad +\sin\phi\frac{h^4a_\odot}{\mu^3}(\cos(\Omega+\omega)\left(2\pi+\left(\frac{\theta}{2}+\frac{\sin2\theta}{4}\right)|_0^{2\pi}-e\sin\theta|_0^{2\pi}-3e\left(\frac{\sin\theta}{3}(\cos^2\theta+2)\right)|_0^{2\pi}\right) \\ &\quad -\sin(\Omega+\omega)\left(\frac{\sin^2\theta}{2}+e\cos^3\theta\right)|_0^{2\pi})\end{aligned} \tag{5.10}$$

Note that the last term in Eq. (5.10) is evaluated to be zero, so for the non-perigee aligned acceleration component Eq. (5.11) applies (where ua stands for the unaligned component).

$$\int_0^T \dot{\omega}_{\mathrm{ua}} \mathrm{d}t = 0 \tag{5.11}$$

Continue to simplify Eq, (5.10) to get Eq. (5.12).

$$\delta e_x = \cos\phi \delta e_{x,\mathrm{id}} + \sin\phi \frac{3\pi h^4 a_\odot \cos(\Omega+\omega)}{\mu^3} \tag{5.12}$$

Plug in the result for the ideally aligned case in Eq. (2.16) to get Eq. (5.13).

$$\delta e_x = \cos\phi(-\frac{3\pi h^4 \sin(\Omega+\omega) a_\odot}{\mu^3}) + \sin\phi \frac{3\pi h^4 a_\odot \cos(\Omega+\omega)}{\mu^3} \tag{5.13}$$

Note the aligned and unaligned components are very similar. Simplifying further, the change in e_x over one day is evaluated as Eq. (5.14).

$$\delta e_x = \frac{3\pi h^4 a_\odot}{\mu^3}(-\cos\phi \sin(\Omega+\omega) + \sin\phi\cos(\Omega+\omega)) \tag{5.14}$$

Therefore the general e_x derivative is approximated by Eq. (5.15).

$$\frac{\mathrm{d}e_x}{\mathrm{d}\theta} = \frac{\delta e_x}{2\pi} = \frac{3h^4 a_\odot}{2\mu^3}(-\cos\phi\sin(\Omega+\omega) + \sin\phi\cos(\Omega+\omega)) \tag{5.15}$$

Plug Eq. (1.2) into Eq. (5.15) and recognize the scale factor is one for this study to get Eq. (5.16).

$$\frac{\mathrm{d}e_x}{\mathrm{d}\theta} = \frac{3h^4}{2\mu^3}\frac{p_\odot \rho A}{m}(-\cos\phi\sin(\Omega+\omega) + \sin\phi\cos(\Omega+\omega)) \tag{5.16}$$

Again, use the assumption that $h^2 = \mu a$ to get the time derivative of e_x in Eq. (5.17), which is then simplified to Eq. (5.18).

$$\dot{e}_x = \frac{\mathrm{d}e_x}{\mathrm{d}\theta}\frac{\mathrm{d}\theta}{\mathrm{d}t} = \frac{-3a^2 p_\odot \rho A}{2\mu m}(\cos\phi\sin(\Omega+\omega) - \sin\phi\cos(\Omega+\omega))n \tag{5.17}$$

$$\dot{e}_x = \frac{-3a^2 p_\odot \rho A}{2\mu m}\sin(\Omega+\omega-\phi)n = -e_N n_\oplus \sin(\Omega+\omega-\phi) \tag{5.18}$$

Again, this matches the literature results since $\alpha_{\mathrm{R}} = \Omega + \omega - \phi$ [12]. Note that the natural eccentricity is the same as Eq. (2.20) as well [12]. When Eq. (5.18) is integrated, Eq. (5.19) results.

$$e_x = e_N \cos(\Omega+\omega-\phi) \tag{5.19}$$

This traces a full circle for $\alpha_{\mathrm{R}} = \Omega + \omega - \phi = 0$ to 2π radians, which corresponds to one year. Therefore the circular eccentricity plane behavior is once again verified. Interestingly, since the sum of Ω, ω, and -ϕ goes from 0 to 2π radians, these values compensate for each other's behavior. This means the ω and ϕ behavior must balance since Ω is shown to be constant. Therefore ϕ is not constant over a year if ω does not track α completely.

5.1.2 Derivation of $\dot{e}_y$ with Perigee Offset

A similar analysis is conducted for e_y. Substitute Eq. (5.4) into Eq. (2.21) to get Eq. (5.20).

$$\begin{aligned}\delta e_y &= \frac{ha_\odot}{\mu}(\sin(\Omega+\omega)\int_0^T\left(\sin\phi+\frac{e+\cos\theta}{1+e\cos\theta}(\sin\theta\cos\phi+\cos\theta\sin\phi)\right)\mathrm{d}t \\ &\quad +\cos(\Omega+\omega)\int_0^T\left(\cos\phi+\frac{\sin^2\theta\cos\phi+\sin\theta\cos\theta\sin\phi}{1+e\cos\theta}\right)\mathrm{d}t) \end{aligned} \tag{5.20}$$

This can be written in terms of the ideally aligned results as Eq. (5.21), which is then simplified to Eq. (5.22).

$$\begin{aligned}\delta e_y &= \cos\phi\delta e_{y,\mathrm{id}}+\sin\phi\frac{ha_\odot}{\mu}(\sin(\Omega+\omega)\int_0^T\left(1+\frac{e+\cos\theta}{1+e\cos\theta}\cos\theta\right)\mathrm{d}t \\ &\quad +\cos(\Omega+\omega)\int_0^T\frac{\sin\theta\cos\theta}{1+e\cos\theta}\mathrm{d}t) \end{aligned} \tag{5.21}$$

$$\begin{aligned}\delta e_y &= \cos\phi\delta e_{y,\mathrm{id}}+\sin\phi\frac{ha_\odot}{\mu}(\sin(\Omega+\omega)\int_0^T\left(1+e\cos\theta+\cos^2\theta-e\cos^3\theta\right)\mathrm{d}t \\ &\quad +\cos(\Omega+\omega)\int_0^T\sin\theta\cos\theta(1-e\cos\theta)\mathrm{d}t) \end{aligned} \tag{5.22}$$

Now switch the integration variable again from time to true anomaly to get Eq. (5.23), which is simplified to Eq. (5.24).

$$\begin{aligned}\delta e_y &= \cos\phi\delta e_{y,\mathrm{id}} \\ &\quad +\sin\phi\frac{h^4a_\odot}{\mu^3}(\sin(\Omega+\omega)\int_0^{2\pi}\left(1+e\cos\theta+\cos^2\theta-e\cos^3\theta\right)(1-2e\cos\theta)\mathrm{d}\theta \\ &\quad +\cos(\Omega+\omega)\int_0^{2\pi}\sin\theta\cos\theta(1-e\cos\theta)(1-2e\cos\theta)\mathrm{d}\theta) \end{aligned} \tag{5.23}$$

$$\begin{aligned}\delta e_y &= \cos\phi\delta e_{y,\mathrm{id}} \\ &+ \sin\phi\frac{h^4 a_\odot}{\mu^3}(\sin(\Omega+\omega)\left(\int_0^{2\pi}\mathrm{d}\theta - e\int_0^{2\pi}\cos\theta\mathrm{d}\theta + \int_0^{2\pi}\cos^2\theta\mathrm{d}\theta - 3e\int_0^{2\pi}\cos^3\theta\mathrm{d}\theta\right) \\ &+ \cos(\Omega+\omega)\left(\int_0^{2\pi}\sin\theta\cos\theta\mathrm{d}\theta - 3e\int_0^{2\pi}\sin\theta\cos^2\theta\mathrm{d}\theta\right)) \end{aligned} \tag{5.24}$$

Solve the integrals to get Eq. (5.25) [20].

$$\begin{aligned}\delta e_y &= \cos\phi\delta e_{y,\mathrm{id}} \\ &+ \sin\phi\frac{h^4 a_\odot}{\mu^3}(\sin(\Omega+\omega)\left(2\pi - e\sin\theta|_0^{2\pi} + \left(\frac{\theta}{2}+\frac{\sin 2\theta}{4}\right)|_0^{2\pi} - 3e\left(\frac{\sin\theta}{3}(\cos^2\theta+2)\right)|_0^{2\pi}\right) \\ &+ \cos(\Omega+\omega)\left(\frac{\sin^2\theta}{3}|_0^{2\pi} + e\cos^3\theta\right)) \\ &= \cos\phi\delta e_{y,\mathrm{id}} + \sin\phi\frac{h^4 a_\odot}{\mu^3}\sin(\Omega+\omega)3\pi \end{aligned} \tag{5.25}$$

Note that Eq. (5.11) is proven again for the unaligned component. Combine Eq. (5.25) with the ideal results in Eq. (2.23) to get Eq. (5.26).

$$\delta e_y = \frac{3\pi h^4 a_\odot}{\mu^3}(\cos\phi\cos(\Omega+\omega)+\sin\phi\sin(\Omega+\omega)) = \frac{3\pi h^4 a_\odot}{\mu^3}\cos(\Omega+\omega-\phi) \tag{5.26}$$

Using Eq. (5.26), the general e_y derivative with respect to true anomaly is calculated in Eq. (5.27).

$$\frac{\mathrm{d}e_y}{\mathrm{d}\theta} = \frac{\delta e_y}{2\pi} = \frac{3h^4 a_\odot}{2\mu^3}\cos(\Omega+\omega-\phi) \tag{5.27}$$

After plugging in Eq. (1.2) with a scale factor of one, Eq. (5.27) becomes Eq. (5.28).

$$\frac{\mathrm{d}e_y}{\mathrm{d}\theta} = \frac{3h^4}{2\mu^3}\frac{p_\odot \rho A}{m}\cos(\Omega+\omega-\phi) \tag{5.28}$$

To find the time derivative of e_y, use the assumption that $h^2 = \mu a$ again to get Eq. (5.29).

$$\dot{e}_y = \frac{\mathrm{d}e_y}{\mathrm{d}\theta}\frac{\mathrm{d}\theta}{\mathrm{d}t} = \frac{3a^2 p_\odot \rho A}{2\mu m}\cos(\Omega+\omega-\phi)n = e_N n_\oplus \cos(\Omega+\omega-\phi) \tag{5.29}$$

This matches the literature results since $\alpha_{\mathrm{R}} = \Omega+\omega-\phi$ [12]. Note that natural eccentricity is once again Eq. (2.20) [12]. When integrated, Eq. (5.29) becomes Eq. (5.30).

$$e_y = e_N \sin(\Omega+\omega-\phi) \tag{5.30}$$

This traces a full circle for $\alpha_{\mathrm{R}} = \Omega + \omega - \phi = 0$ to 2π radians, so the known eccentricity vector behavior is still verified. The main change from the ideal perigee-pointing case to the general perigee offset case is that the eccentricity magnitude is no longer constant due to the unaligned component.

5.1.3 Comparison of Aligned and Unaligned Solar Radiation Pressure Effects

The preceding analysis reveals an intriguing insight into the solar radiation pressure's effect on an orbit's eccentricity vector. For the solar radiation pressure acceleration component aligned with perigee, $\dot{e}$ is zero over one orbit around the Earth and $\dot{\omega}$ is nonzero, while the opposite is true for the unaligned component. Therefore the aligned component of the solar radiation pressure provides the rotation of the eccentricity vector, while the unaligned component of the solar radiation pressure provides the change in eccentricity magnitude. The general orbit behavior is a perigee offset-scaled combination of these two components. This leads to Eq. (5.31) and Eq. (5.32).

$$\begin{aligned} \dot{e} &= \dot{e}_{\mathrm{id}} \cos\phi - \dot{e}_{\mathrm{ua}} \sin\phi \\ \dot{\omega} &= \dot{\omega}_{\mathrm{id}} \cos\phi - \dot{\omega}_{\mathrm{ua}} \sin\phi \end{aligned} \tag{5.31}$$

$$\begin{aligned} \int_0^T \dot{e}_{\mathrm{id}} \mathrm{d}t &= \int_0^T \dot{\omega}_{\mathrm{ua}} \mathrm{d}t = 0 \\ \int_0^T \dot{e}_{\mathrm{ua}} \mathrm{d}t &= e \int_0^T \dot{\omega}_{\mathrm{id}} \mathrm{d}t = \frac{3h^4 a_{\odot} \pi}{\mu^3} \end{aligned} \tag{5.32}$$

5.1.4 Effect on Radius of Periapsis with Perigee Offset

The goal of this analysis is to find the effect of perigee offset errors on the radius of periapsis. Once again, use the Gaussian variational equation to determine the effect of a perigee offset error on the semi-major axis (which for the ideal case remains constant). With the new acceleration terms, Eq. (2.27) because Eq. (5.33), which is simplified to Eq. (5.34).

$$\dot{a} = \frac{2a^2 a_{\odot}}{h} \left(e \sin\theta (-\cos\theta \cos\phi + \sin\theta \sin\phi) + (1 + e\cos\theta)(\sin\theta \cos\phi + \cos\theta \sin\phi) \right) \tag{5.33}$$

$$\dot{a} = \frac{2a^2 a_{\odot}}{h} \left(\sin\theta \cos\phi + \sin\phi (e + \cos\theta) \right) \tag{5.34}$$

Note that the first term is the same as the ideal result in Eq. (2.28) scaled by $\cos\phi$, and will therefore integrate to zero. However, the (scaled) unaligned acceleration effect must be taken into account. The change in semi-major axis for one orbit of the satellite around the Earth is Eq. (5.35).

$$\delta a = 0 + \int_0^T \frac{2a^2 a_\odot}{h} \sin\phi(e + \cos\theta)\mathrm{d}t \tag{5.35}$$

Changing the integration variable from time to true anomaly results in Eq. (5.36).

$$\delta a = \frac{2h^2 a^2 a_\odot \sin\phi}{\mu^2} \int_0^{2\pi} (e + \cos\theta)(1 - 2e\cos\theta)\mathrm{d}\theta \tag{5.36}$$

Once again, the perigee offset angle is assumed constant over one orbit of the satellite around the Earth.

Expanding Eq. (5.36) and assuming $h^2 = \mu a$ while only keeping first-order eccentricity terms results in Eq. (5.37).

$$\delta a = \frac{2a^3 a_\odot \sin\phi}{\mu} \int_0^{2\pi} (e + \cos\theta - 2e\cos^2\theta)\mathrm{d}\theta \tag{5.37}$$

This integral is solved as Eq. (5.38) [20].

$$\delta a = \frac{2a^3 a_\odot \sin\phi}{\mu} \left(e\theta + \sin\theta - 2e\left(\frac{\theta}{2} - \frac{\sin 2\theta}{4}\right)\right) |_0^{2\pi} = 0 \tag{5.38}$$

This shows that the unaligned component of acceleration also does not change the semi-major axis over one orbit of the satellite around the Earth, rendering the semi-major axis constant for this analysis. Therefore the only change in the radius of periapsis over the year is due to the changing eccentricity values. Again, this is dependent on the assumption that the satellite is always in sunlight, which allows the changes accrued over one satellite orbit to cancel each other out [21].

5.2 MATLAB Simulation

Once again, the mathematical analysis results for perigee offset errors are also simulated in MATLAB. To isolate perigee-offset error effects, the natural eccentricity is assumed to be known and the initial eccentricity magnitude is assumed to be exactly set by the operator. Therefore, the eccentricity circle's location in the eccentricity plane is determined by both the real behavior

(R) and the assumed initial conditions (g). This is easily assessed by examining the center of the eccentricity circle, shown in Eq. (5.39) [12].

$$\begin{aligned} X &= e_{x,0} + e_N \cos(\alpha_{\mathrm{R}} - \pi) = e_N \cos(\Omega_0 + \omega_0) - e_N \cos\alpha_{\mathrm{R}} = e_N \cos\alpha_{\mathrm{g}} - e_N \cos\alpha_{\mathrm{R}} \\ &= e_N(\cos\alpha_{\mathrm{g}} - \cos\alpha_{\mathrm{R}}) \\ Y &= e_{y,0} + e_N \sin(\alpha_{\mathrm{R}} - \pi) = e_N \sin(\Omega_0 + \omega_0) - e_N \sin\alpha_{\mathrm{R}} = e_N(\sin\alpha_{\mathrm{g}} - \sin\alpha_{\mathrm{R}}) \end{aligned} \quad (5.39)$$

5.2.1 Single Error Analysis

The first MATLAB simulation looks at an individual perigee offset error and how it affects the radius of periapsis. A 36° error is used to maintain an examination of 10% errors (of 360°). The general results are summarized in Table 5.1. As explained in further detail in Section 5.2.2, the center Y coordinate also changes, so the center Y ratio is the ratio of this coordinate to the natural eccentricity. Analytically, the center X ratio is equal to $1 - \cos\phi$ and the center Y ratio is equal to $-\sin\phi$. However, it is more intuitive to look at Fig. 5.2. Notice that the guessed initial eccentricity is on the x-axis, since the eccentricity vector is assumed to be aligned with the Sun. Since there is actually a 36° angle between the orbit's perigee and the Sun, the center of the eccentricity circle is relocated accordingly. Alternately, the initial eccentricity is at the 36° position on the circle instead of at 0°. Since the length of the eccentricity vector is changing, the eccentricity magnitude is also

Table 5.1: Perigee Offset Eccentricity Summary

Numerator Factor	1
Denominator Factor	1
Perigee Error	36°
Initial e_x	0.00055645
Initial e_y	0
Initial $\|e\|$	0.00055645
Maximum $\|e\|$	0.00090035
Initial Eccentricity Ratio	1
Center X Ratio	0.19098
Center Y Ratio	-0.58779

changing as shown in Fig. 5.3(a). This increases the maximum eccentricity, shown in Table 5.1, which leads to the change in the radius of periapsis shown in Fig. 5.3(b). Note that this behavior is not perfectly sinusoidal because the center of the eccentricity circle is not on the e_x axis. However, the circular behavior is apparent in the sinusoidal behavior of the component derivatives in Fig. 5.4.

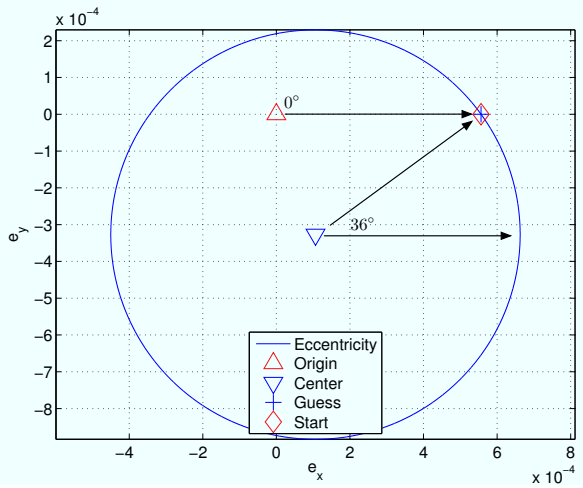

Figure 5.2: Eccentricity Vector Behavior over One Year with a Perigee Offset

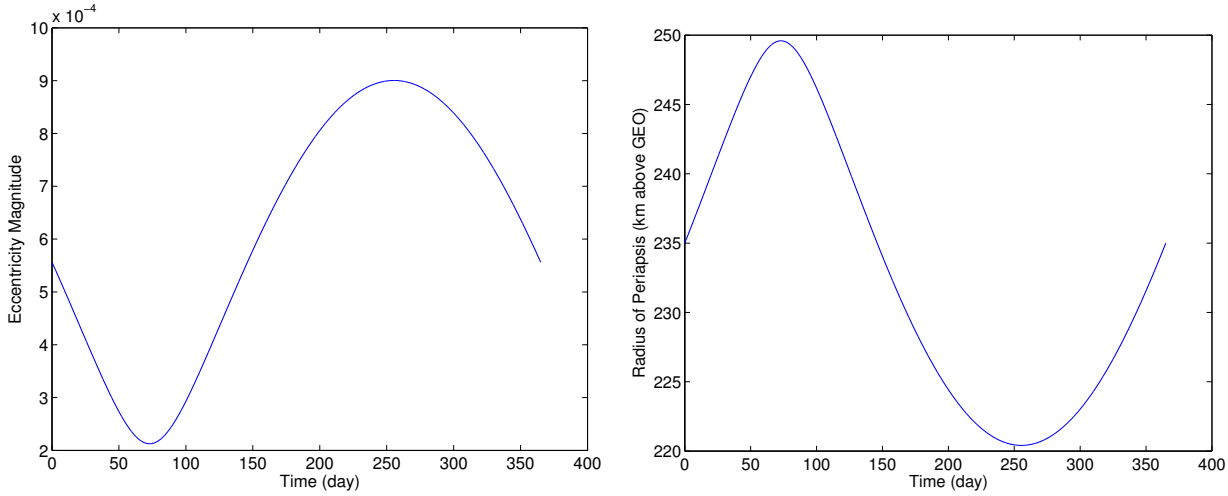

(a) Eccentricity Magnitude

(b) Radius of Periapsis

Figure 5.3: Results from a Perigee Offset

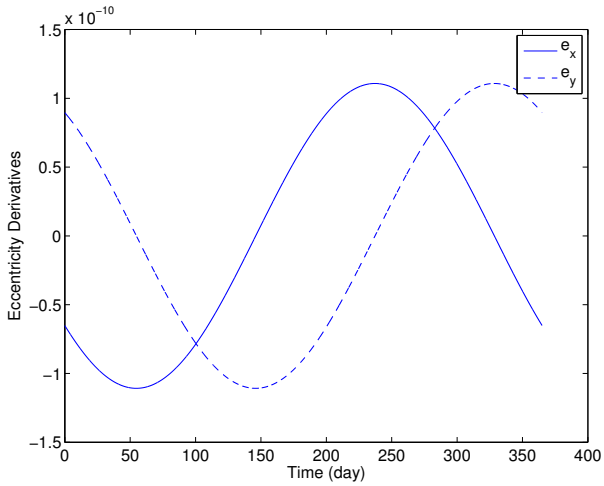

Figure 5.4: Eccentricity Component Derivatives with a Perigee Offset

5.2.2 Monte Carlo Analysis

After examining a single perigee offset error, a Gaussian distribution of perigee offset errors is examined to form a general trend of the resulting radius of periapsis behavior. For this analysis, the Monte Carlo parameters from Chapter 4 were used to create the Gaussian distribution. The standard deviation was set at 36°. Figure 5.5(a) shows the center X ratios for the perigee offsets. This symmetric behavior is not intuitive unless the eccentricity plane is examined as shown in Fig. 5.6. The dotted circle is the targeted eccentricity vector behavior, while the other three circles show perigee offset errors in multiples of 90°. Note that the centers of these circles (and all other possible perigee offset error circles) create a circle themselves (shown in bold). This circle is why the center X ratio behavior is symmetric (assuming the eccentricity magnitude is set exactly). Since the center X ratio behavior is symmetric, its histogram in Fig. 5.5(b) is similar to a one-sided Gaussian distribution. The trendline for the center X ratio, which is very complicated despite this symmetric behavior, is shown in Eq. (5.40). Upon examination, this trendline reflects the trigonometric behavior of the single case analysis for the range of data. (Neither MATLAB or Excel allow the direct formation of trigonometric trendlines.)

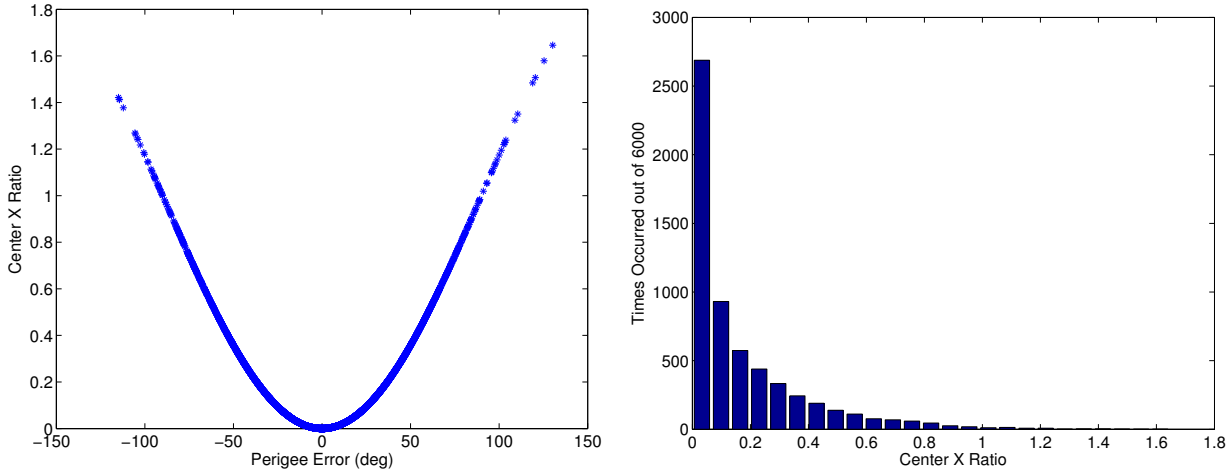

(a) Raw (b) Histogram

Figure 5.5: Center X Ratio Results from Perigee Offset Errors

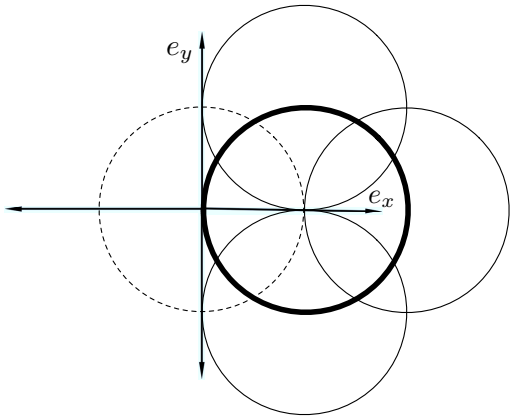

Figure 5.6: Perigee Offset Error Explanation

$$\frac{X_c}{e_N} = 9.2243 \text{ x } 10^{-13}\phi^5 - 3.3076 \text{ x } 10^{-9}\phi^4 - 7.8682 \text{ x } 10^{-9}\phi^3 + 1.5059 \text{ x } 10^{-4}\phi^2 + 1.0709 \text{ x } 10^{-5}\phi + 6.15 \text{ x } 10^{-4} \quad (5.40)$$

Note that since these perigee offset errors are angles, the changes are not limited to just the e_x axis regardless of the right ascension of Sun. Figure 5.7(a) shows the center Y ratio for the perigee offsets, which are described by the trendline in Eq. (5.41). This developed trendline is also a more complicated version of the trigonometric behavior seen in the single error analysis.

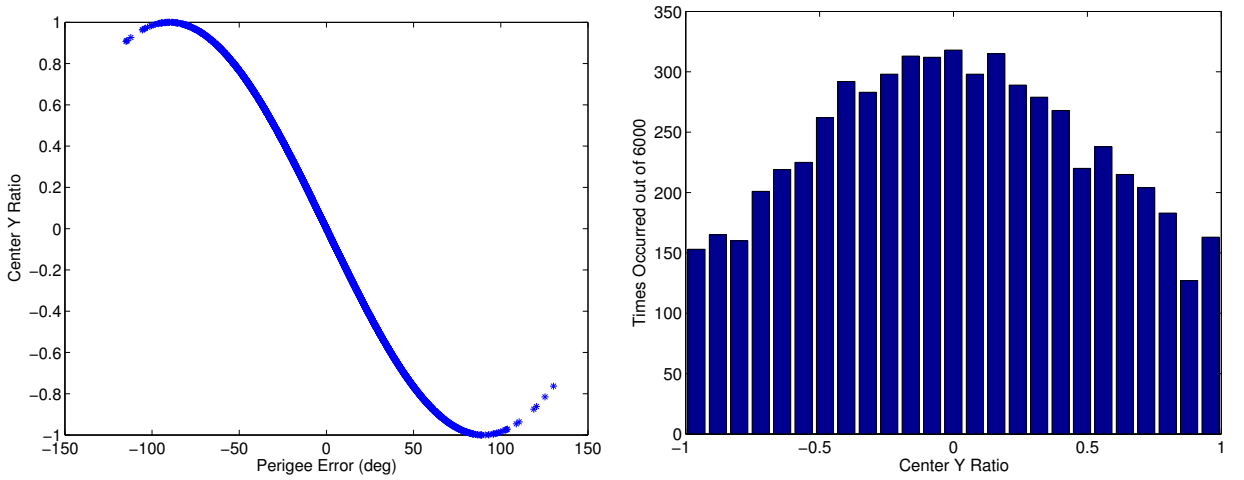

(a) Raw (b) Histogram

Figure 5.7: Center Y Ratio Results from Perigee Offset Errors

Again, the shape of the center Y ratio trend comes from the circle of centers shown in Fig. 5.6. Interestingly, the histogram in Fig. 5.7(b) does not preserve the Gaussian behavior of the error distribution. This is partly because the periodic sinusoidal behavior of the center Y ratio limits its value between -1 and 1, as shown in Fig. 5.7(a).

$$\begin{aligned} \frac{Y_c}{e_N} &= -1.1656 \text{ x } 10^{-11}\phi^5 + 9.1479 \text{ x } 10^{-12}\phi^4 + 8.7717 \text{ x } 10^{-7}\phi^3 \\ &\quad -4.6989 \text{ x } 10^{-8}\phi^2 - 1.7444 \text{ x } 10^{-2}\phi + 2.0366 \text{ x } 10^{-5} \end{aligned} \tag{5.41}$$

Fig. 5.8 shows the maximum eccentricity magnitude for each perigee offset. Any offset in perigee direction increases the maximum eccentricity, as shown in the trendlines for the right and left sides in Eq. (5.42) . As expected from Fig. 5.8, these trendlines oppose each other due to the rotation of the eccentricity circles shown in Fig. 5.6. Also note that Fig. 5.8 shows behavior that is an interesting combination of the center X ratio and the center Y ratio trends.

$$\begin{aligned} |e|_{\text{max,left}} &= 1.1092 \text{ x } 10^{-10}\phi^3 - 9.8827 \text{ x } 10^{-10}\phi^2 \\ &\quad -9.7342 \text{ x } 10^{-6}\phi + 5.5634 \text{ x } 10^{-4} \\ |e|_{\text{max,right}} &= -1.0875 \text{ x } 10^{-10}\phi^3 - 1.2344 \text{ x } 10^{-9}\phi^2 \\ &\quad +9.7412 \text{ x } 10^{-6}\phi + 5.563 \text{ x } 10^{-4} \end{aligned} \tag{5.42}$$

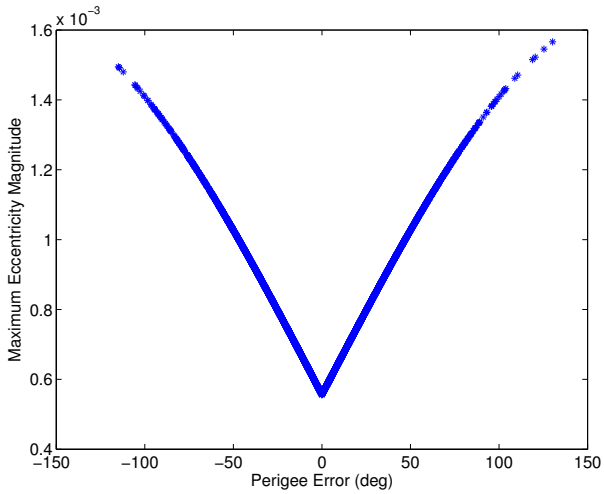

Figure 5.8: Maximum Eccentricity Magnitude from Perigee Offset Errors

Fig. 5.9(a) shows the minimum radius of periapsis for each perigee offset. Again, this behavior opposes the eccentricity behavior due to Eq. (2.26). The trendlines for the left and right sides are shown in Eq. (5.43). Perige offsets of 36° and −36° both decrease the radius of periapsis by 14.6 km. The histogram of the radius of periapsis results, shown in Fig. 5.9(b), shows a half Gaussian-like trend due to this symmetric behavior.

$$\begin{aligned} r_{p\text{min,left}} &= -4.8502 \text{ x } 10^{-9}\phi^4 - 5.6484 \text{ x } 10^{-6}\phi^3 - 1.4999 \text{ x } 10^{-5}\phi^2 \\ &\quad +0.41182\phi - 6.1701 \text{ x } 10^{-4} \\ r_{p\text{min,right}} &= -5.2218 \text{ x } 10^{-9}\phi^4 + 5.7124 \text{ x } 10^{-6}\phi^3 - 1.8414 \text{ x } 10^{-5}\phi^2 \\ &\quad -0.44176\phi - 8.3165 \text{ x } 10^{-4} \end{aligned} \tag{5.43}$$

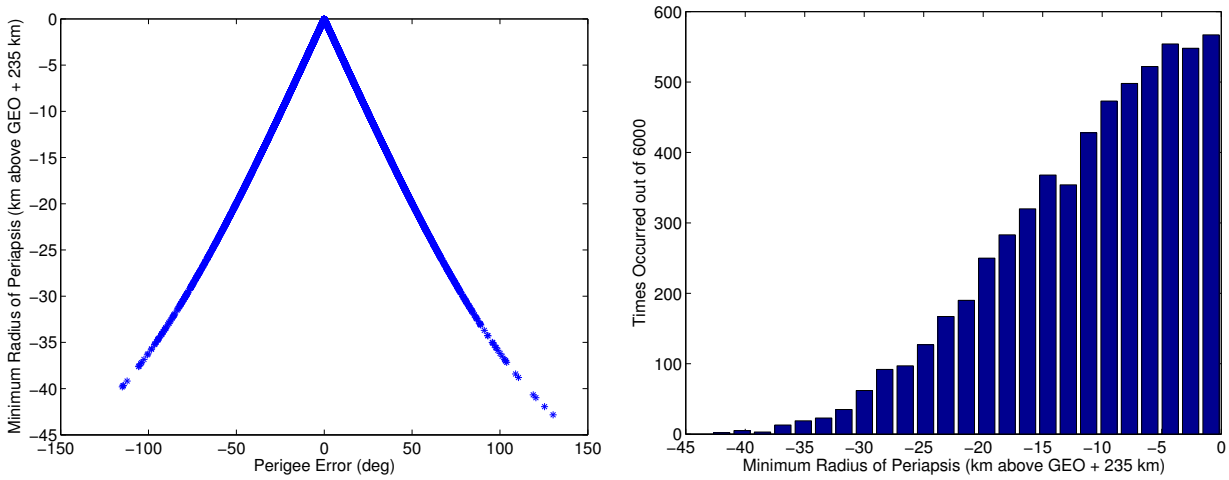

(a) Raw

(b) Histogram

Figure 5.9: Minimum Radius of Periapsis Results from Perigee Offsets

Chapter 6

Conclusions

As discussed in this thesis, operators of an Eurostar 2000 satellite have proposed a new disposal orbit developed to counteract the yearly perturbation due to solar radiation pressure. By aligning the orbit's perigee with the Sun and giving the orbit the satellite's natural eccentricity, the derivative of the eccentricity vector resulting from solar radiation pressure is converted to a change in perigee direction only. The eccentricity magnitude stays the same while the perigee direction rotates around the Earth with the right ascension of the Sun. While the solar radiation pressure perturbation has been discussed previously in literature, it was rigorously verified mathematically by a derivation from Gaussian variational equations and demonstrated through a MATLAB simulation. This simulation also verified the proposed orbit under idealized conditions. NASA's General Mission Analysis Tool was then used to model this orbit under a variety of realistic conditions. While other perturbations added smaller high-frequency perturbations, the radius of periapsis variation was still drastically reduced with the proposed orbit.

This thesis then expanded the analysis to include the sensitivity of this orbit mitigation to different parameters. These errors were divided into three categories, which were modeled with both single errors and Gaussian error distributions. The first dealt with errors in the natural eccentricity calculation. The natural eccentricity is dictated by the solar radiation pressure, reflectivity, area, and mass. All of these except for mass proportionally affected the natural eccentricity, so equal percentage changes led to equal radius of periapsis changes for these parameters (for the same satellite). Mass is inversely proportional to natural eccentricity, so the inverse of its percentage

change was equivalent to the others' percentage changes. Assuming the initial eccentricity can be set exactly, half of these errors do not decrease the radius of periapsis because only increases in natural eccentricity affect the maximum eccentricity. This indicates the maximum natural eccentricity should be used to ensure the desired minimum radius of periapsis.

The second error category disregards the exact initialization assumption and instead assumes perfect knowledge of the natural eccentricity. All initialization errors result in a decrease in the radius of periapsis. Moreover, this reduction is half of the radius of periapsis reduction from the corresponding percentage error in natural eccentricity. However, the same decrease in the radius of periapsis results regardless of whether the error is an increase or decrease of the same percentage.

The third category is errors in pointing the orbit's perigee toward the Sun. The evolution of the orbit was rederived to account for the generic alignment. This showed that the component of solar radiation pressure that is aligned with the perigee direction controls the change in the eccentricity vector direction, while the unaligned component of the solar radiation pressure controls the change in the eccentricity magnitude. Once the known perturbation behavior was again verified, the results of perigee offset errors were modeled in MATLAB. While additional changes in the e_y axis occur since these are angle errors, all errors decreased the radius of periapsis. Therefore while the produced orbit nulls the solar radiation pressure perturbation in the ideal case, margin must be left for errors, especially when absolute knowledge of the satellite's parameters and control of reorbiting does not exist.

This thesis addresses the one-year perturbation due to solar radiation pressure, which is one piece of a much larger puzzle to design disposal orbits. The non-idealized effects of solar radiation pressure need to be investigated over the long term for the proposed orbit before it can be practically used since this derived behavior assumed first-order eccentricity values, no eclipses, and constant parameters. The out-of-plane solar radiation force and inclination variances should also be analyzed for their long-term effects on the overall orbit. Other perturbations, such as luni-solar perturbations or Earth gravitational potential effects, may become larger factors over the long term, slowly shifting an ideally-positioned eccentricity circle away from the eccentricity

plane's origin and decreasing the radius of periapsis. In addition, further sensitivity studies specific to the spacecraft will need to be performed to determine a specific satellite's ability to achieve the necessary eccentricity vector in the disposal orbit on its last bit of fuel. In conclusion, even though this new orbit shows potential for orbit design, there is more analysis to be done before implementing it.

Bibliography

[1] General Mission Analysis Tool (GMAT) Mathematical Specifications DRAFT. NASA Goddard Space Flight Center, Greenbelt, MD, April 2011.

[2] Chia-Chun "George" Chao. Applied Orbit Perturbation and Maintenance. The Aerospace Press, American Institute of Aeronautics and Astronautics, Inc., 2005.

[3] Chia-Chun "George" Chao and Spencer Campbell. Long-term perigee height variations of geo disposal orbits - a revisit. In Proceedings of the Fourth European Conference on Space Debris, volume ESA SP-587. European Space Agency, April 2005.

[4] N. Delong and C. Frémeaux. Eccentricity management for geostationary satellites during end of life operations. In Proceedings of the Fourth European Conference on Space Debris, volume ESA SP-587. European Space Agency, August 2005.

[5] C. Hernández and R. Jehn. Classification of geostationary objects. Space Debris, 1:235–337, 2001.

[6] R. Jehn, G. Agapov, and C. Hernández. The situation in the geostationary ring. Advances in Space Research, 35:1318–1327, March 2005.

[7] Rüdiger Jehn, Vladimir Agapov, and Cristina Hernández. End-of-life disposal of geostationary satellites. In Proceedings of the Fourth European Conference on Space Debris, volume SP-587. European Space Agency, August 2005.

[8] Heiner Klinkrad. Space Debris - Models and Risk Analysis. Springer Praxis Publishing Ltd., Chichester, UK, 2006.

[9] H.G. Lewis, G.G. Swinerd, C.E. Martin, and W.S. Campbell. The stability of disposal orbits at super-synchronous altitudes. Acta Astronautica, 55(299-310):12, 2004.

[10] Swiss Reinsurnace Company Ltd. Space debris: On collision course for insurers? Report, 2011.

[11] Khánh Kim Luu. Effects of Perturbations on Space Debris in Supersynchronous Storage Orbits. PhD thesis, University of Colorado Boulder, 1998.

[12] Gérard Maral and Michel Bousquet. Satellite Communications Systems: Systems, Techniques and Technology. John Wiley and Sons, Ltd., Chichester, West Sussex, United Kingdom, fifth edition, 2009.

[13] David Mignon, Franck Raballand, Jean-Louis Gonnaud, and Sophie Jallade. Eurostar 2000 disposal on a graveyard orbit: Orbit control strategy and operational implementation. In Proceedings of the 18th International Symposium on Space Flight Dynamics, volume SP-548, pages 79–84. German Space Operations Center of DLR and European Space Operations Centre of ESA, 2004.

[14] David S. Moore. The Basic Practice of Statistics. W. H. Freeman and Company, New York, NY, fifth edition, 2010.

[15] NASA Orbital Debris Program Office. Geo image. NASA Orbital Debris Program Office Photo Gallery, http://orbitaldebris.jsc.nasa.gov/photogallery/beehives/GEO1280.jpg, October 2012.

[16] Joe Rao. Spring Arrives with Equinox Tuesday, Earliest in Over a Century. SPACE.com, March 2012.

[17] Guy Richards. An orbital graveyard. Engineering and Technology, Control Satellite:36–40, April 2010.

[18] A. Rolfo. Space debris mitigation: Contribution and proposals. In Proceedings of the Second European Conference on Space Debris, volume SP-393, pages 677–680, May 1997.

[19] A. Rossi, L. Anselmo, A. Cordelli, P. Farinella, and C. Pardini. Modelling the evolution of the space debris population. Planet. Space Sci., 46(11/12):1583–1596, 1998.

[20] James Stewart. Calculus. Brooks/Cole, Belmont, California, fifth edition, 2003.

[21] David A. Vallado. Fundamentals of Astrodynamics and Applications. Space Technology Library. Microcosm Press and Springer, Hawthorne, CA and New York, NY, third edition, 2007.

[22] Mark Wade. Encyclopedia astronautica: Eurostar 2000, http://www.astronautix.com, February 2013.

[23] Ulrich Walter. Astronautics. WILEY-VCH Verlag GmbH and Co. KGaA, Weinheim, Germany, 2008.

Appendix A

Further Investigation into GMAT behavior

As demonstrated in Chapter 3, there are trends in the eccentricity and the radius of periapsis behavior that are unaccounted for by the derived solar radiation pressure perturbation. These effects are isolated and compared in the simulations below. The following simulations use the proposed orbit parameters.

A.1 J2 Effects

The first effect isolated is the J2 effect. The Earth's point mass creates a constant orbit that does not change its shape or orientation in space. The oblateness of the Earth causes high-frequency variations in the eccentricity, and therefore the radius of periapsis due to Eq. (2.26). These changes are relatively small and fast compared to the analyzed solar radiation pressure perturbation, so over a year it appears as a "band" of results around the average behavior, as seen in Fig. A.1(a) and Fig A.1(b).

A.2 Full Gravity Model Effects

After examining the J2 results, all of the Earth's gravitational model is included in the simulation. The Joint Gravity Model-2 Degree 8 Order 8 model is used in this thesis. Figure A.2(a) shows a slight variation in the eccentricity bounds, but Fig. A.2(b) implies that there are also periodic variations in the semi-major axis. Once again, these perturbations are smaller than the solar radiation pressure perturbation the proposed orbit is designed to overcome.

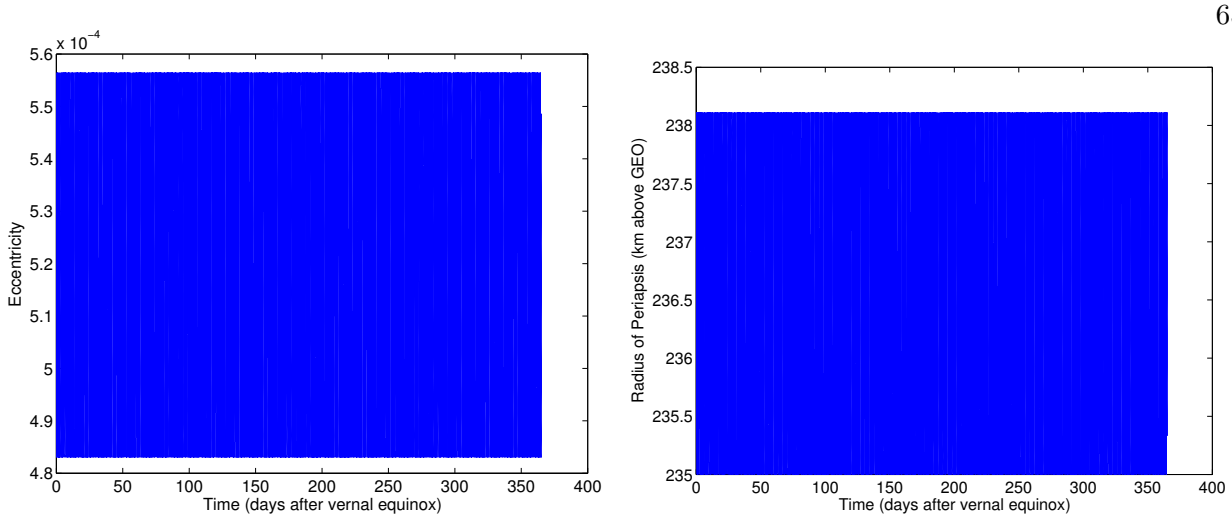

(a) Eccentricity Magnitude (b) Radius of Periapsis

Figure A.1: Results with J2 Effect Only

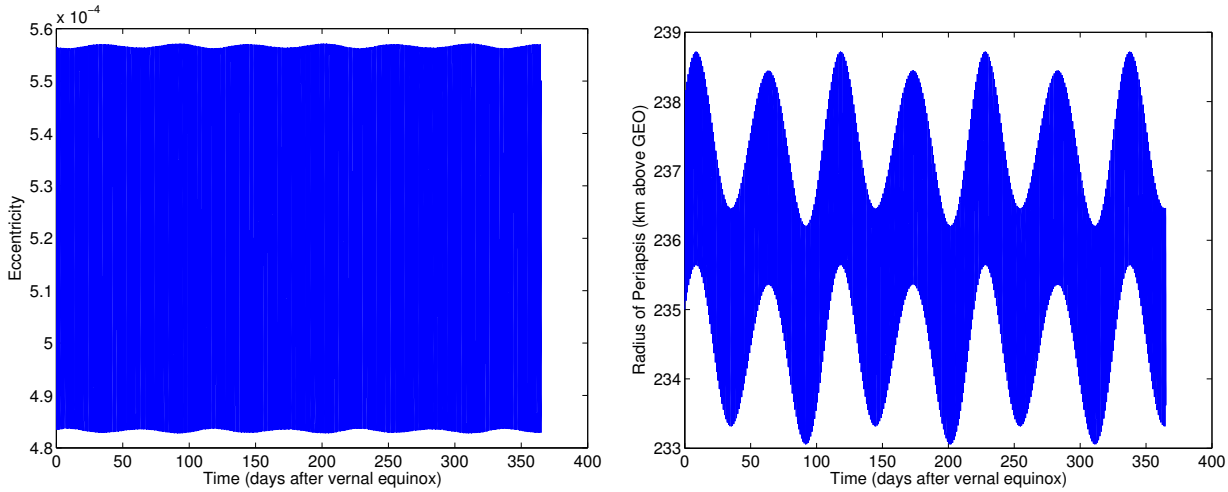

(a) Eccentricity Magnitude (b) Radius of Periapsis

Figure A.2: Results with Full Gravity Model

A.3 Third Body Effects

Next, the third body effects of the Sun and the Moon are isolated and analyzed. As seen in Fig. A.3(a) and Fig. A.3(b), these effects are more random than the gravitational effects, although general periodic patterns and a slight secular slope are seen (this is a part of a longer periodic effect).

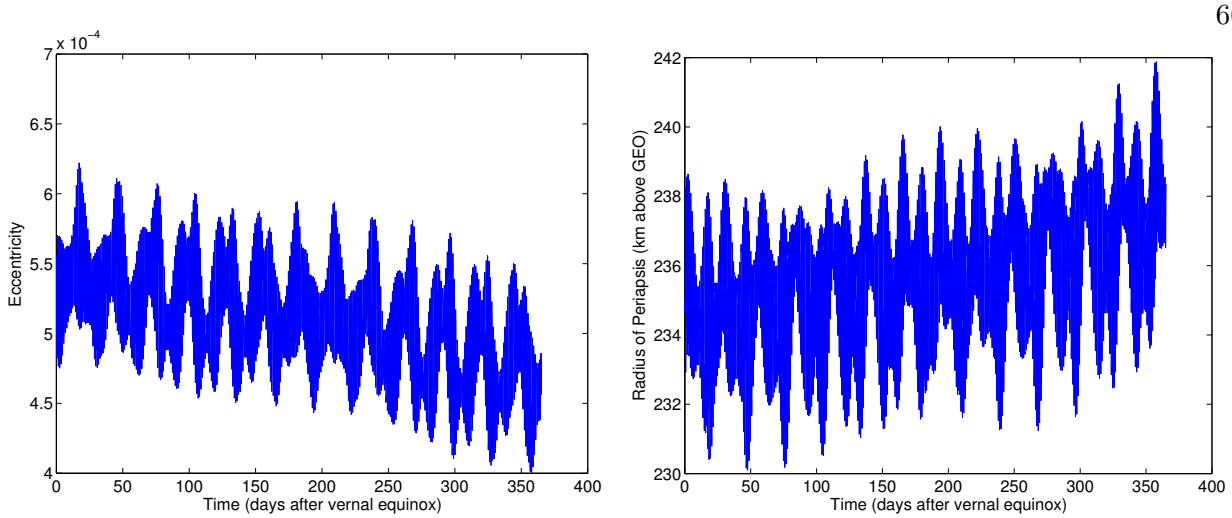

(a) Eccentricity Magnitude

(b) Radius of Periapsis

Figure A.3: Results with Third Body Effects

Again, these perturbations are smaller than the solar radiation pressure perturbation analyzed in this thesis.

A.4 Out-of-Plane Solar Radiation Pressure Effects

Finally, an interesting trend occurs when just solar radiation pressure and the Earth's point mass are used to propagate the proposed orbit. The eccentricity and radius of periapsis results are shown in Fig. A.4(a) and Fig. A.4(b). This additional perturbation is from the solar radiation pressure, but is smaller than the original examined solar radiation pressure effect (which is nulled by the proposed orbit). Since this perturbation is also a yearly periodic effect, the most probable explanation is the 23.44° angle between the equator and the ecliptic plane. [12] This causes a small part of the solar radiation pressure to act out of the orbital plane, causing this effect. Since the extra perturbation is so much smaller than the analyzed solar radiation perturbation, it is not analyzed in this thesis. In fact, it often is masked by other perturbations as seen in Fig. 3.6(a) and Fig. 3.6(b).

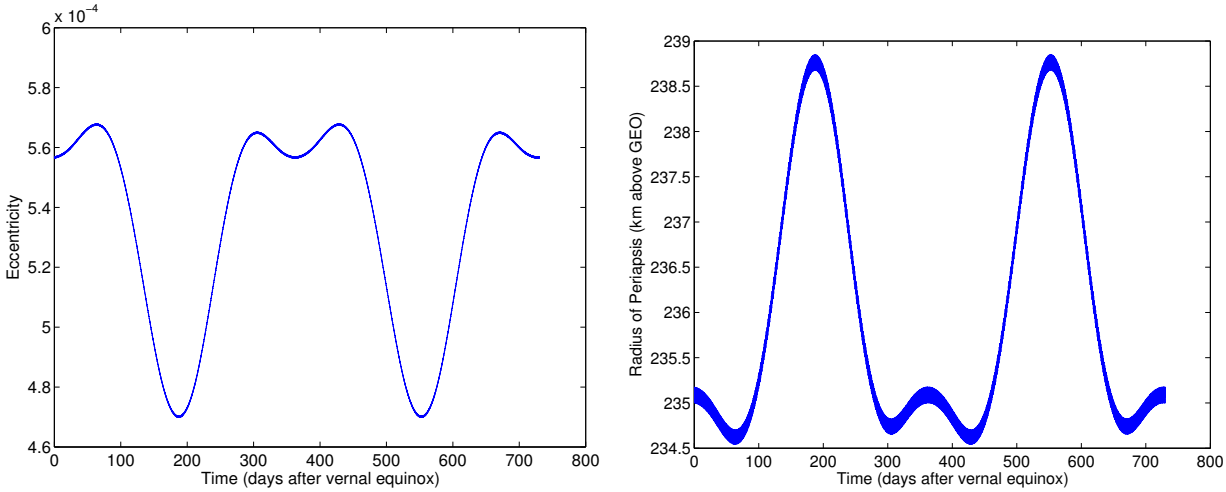

(a) Eccentricity Magnitude

(b) Radius of Periapsis

Figure A.4: Results with "Corrected" Solar Radiation Pressure